

# Locating Boosted Kerr and Schwarzschild Apparent Horizons.

Mijan F. Huq<sup>(1)</sup>, Matthew W. Choptuik<sup>(2)</sup> and Richard A. Matzner<sup>(3)</sup>

<sup>(1)</sup>*Department of Astronomy & Astrophysics and Center for Gravitational Physics & Geometry,  
The Pennsylvania State University, University Park, PA 16803*

<sup>(2)</sup>*Department of Physics and Astronomy,  
University of British Columbia, Vancouver BC, V6T 1Z1, Canada,*

<sup>(3)</sup>*Center for Relativity,  
The University of Texas at Austin, Austin, TX 78712-1081*

We describe a finite-difference method for locating apparent horizons and illustrate its capabilities on boosted Kerr and Schwarzschild black holes. Our model spacetime is given by the Kerr-Schild metric. We apply a Lorentz boost to this spacetime metric and then carry out a 3+1 decomposition. The result is a slicing of Kerr/Schwarzschild in which the black hole is propagated and Lorentz contracted. We show that our method can locate distorted apparent horizons efficiently and accurately.

## I. INTRODUCTION

Apparent horizon locators play an integral role in the application of black hole excision techniques in the computational evolution of black hole spacetimes. Excision techniques delete the regions of spacetime that contain the curvature singularity from the computational domain. Assuming cosmic censorship, these curvature singularities are expected to be contained within an event horizon. The event horizon is a causal boundary whose interior does not causally affect the exterior spacetime; as a result it is possible to excise a region within the event horizon, thereby excising the black hole's curvature singularity.

In our approach to computationally solving the Einstein field equations we focus on the use of Cauchy techniques, in which a 3+1 splitting of spacetime into a foliation of spacelike hypersurfaces,  $\Sigma$ , parametrized in time, is the basis for an evolution in time. The result of this splitting is a system of elliptic and hyperbolic partial differential equations in the 3-metric,  $\gamma_{ij}$ , and extrinsic curvature,  $K_{ij}$ . These are the four constraint equations and 12 first-order-in-time evolution equations. The Cauchy approach starts with an initial spacelike slice with  $\gamma_{ij}$  and  $K_{ij}$  set by solving an initial value problem (the elliptic constraint equations). One then uses the evolution equations to evolve to the next spacelike slice obtaining  $\gamma_{ij}$  and  $K_{ij}$  at the next time (See York [1] for a detailed discussion).

In the evolution of black hole spacetimes in this manner we do not have a complete history of the entire spacetime and hence do not have a knowledge of the location of the event horizon. Since the event horizon is a global object that depends on geometric information for all time (or at least until the black hole becomes quiescent) we cannot use it to determine an inner excision boundary in our Cauchy evolution. There is, however, an alternative, and that is to use the apparent horizon surface which is a local object, locatable (if it exists)

with  $\gamma_{ij}$  and  $K_{ij}$  at one time. The apparent horizon is the outermost marginally trapped surface. It is a closed spacelike 2-surface whose future-directed outgoing null normals have zero divergence [2]. The apparent horizon is slicing dependent and may not necessarily exist even though an event horizon does. An example of this is given by Wald and Iyer [3] through nonspherically-symmetric slicings for the Schwarzschild spacetime. Provided a *non-pathological* slicing is chosen the apparent horizon or any trapped surface within it may be used for excising the black hole singularity. These surfaces define a local causal structure that distinguishes instantaneously escaping null rays from those that are certain to collapse. This distinction makes their treatment very amenable to computational black hole excision techniques. Since these surfaces can be determined with geometric information at one instant of time, they are used in practice as an inner boundary in Cauchy evolutions. With this purpose in mind, we developed a 3D apparent horizon locator that utilizes  $\gamma_{ij}$  and  $K_{ij}$  on a given spacelike slice of spacetime and locates an apparent horizon. Once the apparent horizons are located, a region contained within the apparent horizon is excised. Thus the method is really a trapped-surface excision.

There has been a variety of work done on apparent horizon location in spherical symmetry, axisymmetry and 3D. We focus solely on the 3d locators. These can be classified into those that use finite difference methods, and those that utilize pseudo-spectral schemes. Further, one can classify each of these finders in terms of those that use flow methods versus those that directly solve the apparent horizon equation either via a minimization scheme or Newton's method for root finding.

One of the first published 3d apparent horizon locators was developed by Nakamura, Kojima and Oohara [4]. Their method expands the *apparent horizon shape function*,  $r = \rho(\theta, \phi)$  in spherical harmonics to some maximum  $l = l_{max}$ :

$$\rho(\theta, \phi) = \sum_{l=0}^{l_{max}} \sum_{m=-l}^l a_{lm} Y_{lm}(\theta, \phi). \quad (1)$$

With this expansion Nakamura et al. evaluate the apparent horizon equation and solve for the coefficients  $a_{lm}$  via a “direct” functional iteration scheme. Kembal and Bishop [5] reimplemented this approach and made modifications that led to improved convergence and stability behaviour. Anninos et al. [6] and Baumgarte et al. [7] implement similar methods that involve an expansion of  $\rho(\theta, \phi)$ ; the primary differences being that they expand in terms of symmetric trace-free tensors and use Powell’s method for minimization of the square of the apparent horizon equation, Eq.(2) below (which is related to the expansion of the outgoing null normals).

Thornburg [8] gives a very good treatise on the use of finite differencing to solve the apparent horizon equation using spherical coordinates  $(r, \theta, \phi)$  via Newton’s method. He discusses in general how algebraic Jacobians may be applied in a full 3D context. His implementation for horizon finding however is axisymmetric; his full 3-d finder suffers from problems with the z-axis ( $\theta = 0, \pi$ ). Our method for finding horizons uses closely related concepts except that we finite difference in cartesian coordinates, eliminating any potential z-axis problems.

Another class of apparent horizon locators casts the elliptic apparent horizon equation into a parabolic one as suggested by Tod [9], who suggested the use of flow methods in locating apparent horizons. Bernstein [10] implemented Tod’s algorithm in axisymmetry using finite differences, but encountered problems with differencing on a sphere in spherical coordinates in the general case.

The advantage to flow-methods is that one can start with an arbitrary initial guess and flow towards the apparent horizon(s). In some implementations it is possible to find multiple apparent horizon surfaces starting from a single initial guess surface (i.e., there is a topology change in the course of location of the apparent horizon). Pasch [11] uses a level-set method to locate multiple apparent horizons in 3d. He demonstrates his method utilizing time-symmetric conformally flat initial data for multiple black holes. An hybrid flow/level-set-like method utilizing our approach to evaluating the outgoing null expansions via Cartesian finite differences has been implemented by Shoemaker et al. [12]. That method flows towards the apparent horizon(s) from an arbitrary initial guess allowing for topology changes. Gundlach [13] has implemented a “fast flow” method for finding apparent horizons.

In the sections that follow we give a brief discussion of the algorithm used and relegate the details to the appendices. The model spacetime in which all of the results are presented is discussed in section III. In section IV we discuss tests of the algorithm and demonstrate that for distorted apparent horizons for boosted Kerr black holes the algorithm fairs well.

## II. BOUNDARY VALUE PROBLEM APPROACH

On a particular 3D spacelike hypersurface,  $\Sigma$ , from our foliation of spacetime we are given the 3-metric,  $\gamma_{ij}$  and the extrinsic curvature,  $K_{ij}$ . Let  $\mathcal{S}$  be a closed 2-surface in  $\Sigma$ . At any point  $p$  on  $\mathcal{S}$  we can define a spacelike normal,  $s^a$ , to  $\mathcal{S}$ , and a time-like normal,  $n^a$ , to  $\Sigma$ . From these we can construct the outgoing null normal,  $k^a$ , at  $p$ . If the divergence  $\nabla_a k^a$  ( $\nabla_a$  is the covariant derivative compatible with the spacetime metric,  $g_{ab}$ ) is zero *everywhere* on  $\mathcal{S}$ , then  $\mathcal{S}$  is a *marginally trapped surface* (MTS). The apparent horizon is the outermost such MTS. The expansion of the outgoing null normals,  $\nabla_a k^a = 0$ , can be rewritten as an equation entirely in terms of quantities in  $\Sigma$  [1]:

$$D_i s^i + K_{ij} s^i s^j - K = 0. \quad (2)$$

Here  $D_i$  is the covariant derivative compatible with the 3-metric  $\gamma_{ij}$  and  $K$  is the trace of the extrinsic curvature.

The apparent horizon equation is an elliptic partial differential equation on  $\mathcal{S}$  (for a function of coordinates on  $\mathcal{S}$ ). This can be made apparent by noting that an MTS is a closed 2-surface; spherical coordinates are a natural set of coordinates for  $\mathcal{S}$ . The location of  $\mathcal{S}$  can then be written as the radial distance from the origin of the coordinate system,  $r = \rho(\theta, \phi)$ . In general one can generate a foliation of such closed spacelike 2-surfaces based on the distance from the MTS. This is given by

$$\varphi = r - \rho(\theta, \phi), \quad (3)$$

where the  $\varphi = 0$  level surface is the MTS. From  $\varphi$  we define a spacelike vector field, the normal

$$s^i = \gamma^{ij} \partial_j \varphi / \sqrt{\gamma^{kl} \partial_k \varphi \partial_l \varphi}, \quad (4)$$

at every point on these level surfaces. Substituting this into Eq.(2) results in a second order elliptic partial differential equation on  $\mathcal{S}$ ,

$$\begin{aligned} F[\rho] = & \gamma^{ab} \partial_a \partial_b \varphi + \gamma^{ab}{}_{,a} \partial_b \varphi - \frac{1}{2} \omega^{-1} \gamma^{ab} \gamma_{ab}{}^{cd} \partial_b \varphi \partial_c \varphi \partial_d \varphi \\ & - \omega^{-1} \gamma^{ab} \gamma^{cd} \partial_b \varphi \partial_a \partial_c \varphi \partial_d \varphi + \Gamma_{ab}^a \gamma^{bc} \partial_c \varphi \\ & + \omega^{-\frac{1}{2}} K_{ab} \gamma^{ac} \gamma^{bd} \partial_c \varphi \partial_d \varphi - \omega^{\frac{1}{2}} K = 0, \end{aligned} \quad (5)$$

where  $\omega = \gamma^{cd} \partial_c \varphi \partial_d \varphi$  and  $\Gamma_{bc}^a$  is the connection coefficient associated with the 3-metric  $\gamma_{ab}$ .

Our approach involves casting Eq.(5) as a boundary value problem on  $\mathcal{S}$ . As stated, points on  $\mathcal{S}$  are parametrized in spherical coordinates ( $\theta \in [0, \pi], \phi \in [0, 2\pi)$ ).  $\mathcal{S}$  is discretized into an uniform mesh,  $\hat{\mathcal{S}}$ , of  $N_\theta \times N_\phi$  points where  $N_\theta = N_\phi = N_s$ . The domain on  $\hat{\mathcal{S}}$  is ( $0 \leq \theta \leq \pi; 0 \leq \phi < 2\pi$ ) where at the poles,  $\theta = 0, \pi$  all  $N_\phi$  points are identified as one. The  $\phi = 2\pi$  branch cut is identified with the  $\phi = 0$  line. The boundary conditions simply are periodicity at  $\phi = 2\pi$  and  $\phi$  identification at  $\theta = 0, \pi$ . These boundary conditions

are key to avoiding the coordinate singularities at the poles in combination with using *Cartesian* coordinates to discretize partial derivatives on  $\hat{S}$ . We treat  $\varphi$  as a function of Cartesian coordinates  $x, y, z$  and center on each mesh point of  $\hat{S}$  a 3-D Cartesian difference stencil of 27 points. Using the form Eq.(3) we interpolate values of  $\varphi(x, y, z)$  onto each of the 26 stencil points surrounding each  $\hat{S}$  stencil point. (See the appendix for more details.) Using this difference stencil we can evaluate first, second and mixed derivatives of  $\varphi(x, y, z)$  as required by the discretized version of Eq.(5). At every point on  $\hat{S}$  we then construct the residual  $\hat{F}[\rho]$  on  $\hat{S}$  (Note that the discrete version of a continuum quantity,  $T$ , is denoted by,  $\hat{T}$ ).

The problem at hand is to solve for a  $\rho$  that yields  $F[\rho] = 0$ . Since  $F[\rho]$  is a nonlinear operator (as shown in Eq.(5)), we use Newton's method to solve for  $\rho$ . Given an initial guess surface,  $\rho = \rho_0$ , we wish to find a  $\delta\rho$  (the change in the surface) that leads to  $F[\rho_0 + \delta\rho] = 0$  or, to lowest order,

$$F[\rho_0 + \delta\rho] = F[\rho_0] + \left. \frac{\partial F[\rho]}{\partial \rho} \right|_{\rho=\rho_0} \delta\rho + O(\delta\rho^2) = 0. \quad (6)$$

The Jacobian of  $F[\rho]$  is defined to be

$$J \equiv \frac{\partial F}{\partial \rho}. \quad (7)$$

In the discretized case,  $\hat{J}$  is an  $N \times N$  matrix, where  $N$  is the total number of points used in the discretization. To obtain a  $\delta\rho$  that leads to  $F[\rho + \delta\rho] = 0$  we must solve,

$$J \cdot \delta\rho = -F[\rho] \quad (8)$$

for  $\delta\rho$ .

Computationally our tasks are to first evaluate the discrete form of the Jacobian matrix,  $\hat{J}$  and second to solve the discrete form of Eq.(8). We numerically compute the Jacobian matrix by perturbing the surface pointwise and examining the effect of the perturbation on the residual,  $\hat{F}$ . Let  $\bar{\mu}$  denote "independent" points in the computational mesh,  $\hat{S}$ . By independent we mean the unique points (points modulo boundary identification) on  $\hat{S}$ . In particular from the identifications made earlier, there are  $N_s^2 - 2N_s + 2$  independent points in  $\hat{S}$ .  $N_s = N_\theta = N_\phi$  points at each of the poles are treated as one point.  $\bar{\mu} = 1$  represents the  $\theta = 0$  point for all the  $N_\phi$  points ( $0 \leq \phi < 2\pi$ ) and  $\bar{\mu} = N_s^2 - 2N_s + 2$  is the  $\theta = \pi$  point. Eq.(8) then becomes a linear system of equations where  $\hat{J}$  is a  $(N_s^2 - 2N_s + 2) \times (N_s^2 - 2N_s + 2)$  matrix and  $\hat{F}$  and  $\delta\hat{\rho}$  are vectors of length  $N_s^2 - 2N_s + 2$ . The  $\bar{\mu}\bar{\nu}$  component of the Jacobian is then computed by perturbing  $\rho$  at the  $\bar{\nu}$ -th point and computing the change in the residual,  $\hat{F}$  at the  $\bar{\mu}$ -th point. Using a first order forward difference approximation we have,

$$\hat{J}_{\bar{\mu}\bar{\nu}} = \frac{1}{\epsilon} \left\{ \hat{F}_{\bar{\mu}}[\hat{\rho}_{\bar{\mu}} + \epsilon] - \hat{F}_{\bar{\mu}}[\hat{\rho}_{\bar{\nu}}] \right\}, \quad (9)$$

where  $\epsilon$  is the amount by which we perturb the surface. We define  $\epsilon$  to be the *perturbation parameter*. The process for generating the components then involves numerically evaluating  $\hat{F}$  in only a small neighborhood of the  $\nu$ -th point since  $\hat{F}$  has a domain of dependence dependent on the finite difference operators used. In this case the operators are (finite difference) derivative operators convolved with interpolation operators.

The solution of Eq.(8) is achieved via Newton's method. We solve for the change  $\delta\hat{\rho}$  that leads to a new surface  $r = \hat{\rho}_*(\theta, \phi)$  that yields  $\hat{F}[\hat{\rho}_*] \sim 0$  up to  $O(h^2)$ , where  $h$  is the Cartesian stencil spacing, proportional to  $\delta\theta$ . Newton's method then involves updating  $\hat{\rho}(\theta, \phi)$  by  $\delta\hat{\rho}$ . If  $F$  were a linear operator then one iteration would result in a  $\delta\hat{\rho}$  that leads to a solution. Since  $F$  is nonlinear we have to iterate until the  $L_2$ -norm of the residual,  $\|\hat{F}\|_2$ , is driven down to a chosen stopping criterion. We discuss the implementation details in the appendices and discuss further the properties of the Jacobian and Newton's method in the results section. We now turn our attention to the model spacetime in which we shall conduct our numerical experiments.

### III. 3+1 SPLITTING OF THE KERR-SCHILD METRIC

In the rest of the paper we focus on tests of the algorithm based on boosted Schwarzschild and Kerr black holes. The particular form that we use is given by the Kerr-Schild metric:

$$g_{\mu\nu} = \eta_{\mu\nu} + 2Hl_\mu l_\nu, \quad (10)$$

where  $l_\mu$  is an ingoing null vector (i.e:  $g^{\mu\nu}l_\mu l_\nu = \eta^{\mu\nu}l_\mu l_\nu = 0$ ),  $H$  is a scalar function of the spacetime coordinates and  $\eta_{\mu\nu}$  is the Minkowski spacetime metric. This metric describes the Kerr and Schwarzschild spacetimes. We note that under a Lorentz transformation the spacetime metric is form invariant. By definition such a transformation takes  $\eta_{\mu\nu} \rightarrow \eta_{\mu\nu}$  and  $l^\mu$  and  $H$  are transformed to a new null vector and left unchanged (though evaluated at the new coordinate labels for the same event) respectively. This property makes our analysis easier since a 3+1 decomposition of Eq.(10) has the same form as a 3+1 decomposition of the boosted metric. As we shall see, we only need to specify  $H$ ,  $l_\mu$  and their spacetime derivatives in order to obtain the 3-metric and extrinsic curvature on  $\Sigma$ .

For a vacuum spacetime,  $l^\mu$  is geodesic and in the Kerr and Schwarzschild spacetimes is the tangent to geodesics of ingoing photons. The null nature of Eq.(10) leads to a slicing of these spacetimes that is well behaved at the horizon. That is, spacelike slices penetrate the horizon and hit the black hole singularity. This is a desirable property for black hole excision in computational applications and this metric has shown itself to be a good

choice for the study of single and multiple black hole evolutions with excision.

For the Kerr spacetime,  $H$  and  $l_\mu$  are given by

$$H = \frac{Mr^3}{r^4 + a^2 z^2} \quad (11)$$

and

$$l_\mu = \left( 1, \frac{rx + ay}{r^2 + a^2}, \frac{ry - ax}{r^2 + a^2}, \frac{z}{r} \right), \quad (12)$$

where  $r$  is given by

$$\frac{x^2 + y^2}{r^2 + a^2} + \frac{z^2}{r^2} = 1, \quad (13)$$

or

$$r^2 = \frac{1}{2}(\rho^2 - a^2) + \sqrt{\frac{1}{4}(\rho^2 - a^2)^2 + a^2 z^2}. \quad (14)$$

$M$  is the mass of the Kerr black hole and  $a = J/M$  is the angular momentum of the black hole and  $\rho = \sqrt{x^2 + y^2 + z^2}$ .

In the  $a \rightarrow 0$  limit we get the Schwarzschild metric in ingoing Eddington-Finkelstein coordinates where

$$H = \frac{M}{r}, \quad (15)$$

$$l_\mu = \left( 1, \frac{x}{r}, \frac{y}{r}, \frac{z}{r} \right) \quad (16)$$

and  $r = \sqrt{x^2 + y^2 + z^2}$ .

In a spacelike slice of either Kerr or Schwarzschild spacetimes the apparent horizon is known to coincide with the intersection of the event horizon with that slice. In the Kerr spacetime then the apparent horizon is a surface of radius  $r = r_+$ :

$$r_+ = M + \sqrt{M^2 - a^2} \quad (17)$$

and area

$$A = 4\pi(r_+^2 + a^2). \quad (18)$$

In the more general nonstationary case the apparent horizon and event horizon will not coincide. We use the properties of the Kerr and Schwarzschild spacetimes to test out our method for finding horizons.

To get the spacetime metric for a boosted black hole consider  $\mathcal{O}$  to be the rest frame of the black hole, with coordinates  $(\bar{t}, \bar{x}^i)$ . Let  $\mathcal{O}$  be another stationary frame with coordinates  $(t, x^i)$  such that  $\mathcal{O}$  is related to  $\bar{\mathcal{O}}$  via a Lorentz boost along the  $\hat{v} = (v_x, v_y, v_z)$  direction: in the  $\mathcal{O}$  frame the black hole moves in the  $\hat{v}$  direction with boost velocity,  $v$  ( $\delta_{ij}\hat{v}^i\hat{v}^j = 1$ ). As usual, we define  $\gamma = 1/\sqrt{1 - v^2}$ .  $H(x_\mu)$  and  $l_\mu$  (bar denoting  $\bar{\mathcal{O}}$  frame) now transform as

$$H(x_\mu) = H(\Lambda_{\mu\bar{\nu}}^{\bar{\nu}} x_{\bar{\nu}}) \quad (19)$$

and

$$l_\mu = \Lambda_{\mu\bar{\nu}}^{\bar{\nu}} l_{\bar{\nu}}(\Lambda_{\bar{\gamma}\sigma}^{\sigma} x_{\bar{\sigma}}). \quad (20)$$

These preserve the form of (10).

### A. 3+1 Decomposition

The standard ADM 3+1 form of the spacetime metric is given by

$$ds^2 = -\alpha^2 dt^2 + \gamma_{ij} (dx^i + \beta^i dt) (dx^j + \beta^j dt) \quad (21)$$

If we compare (10) to (21) and use the property that  $l^\mu l_\mu = 0$ , we find that the lapse is given by

$$\alpha = \frac{1}{\sqrt{1 + 2Hl_t^2}}, \quad (22)$$

and the shift is given by

$$\beta_i = 2Hl_t l_i \quad (23)$$

or

$$\beta^i = 2Hl_t \delta^{ij} l_j / (1 + 2Hl_t^2). \quad (24)$$

The 3-metric is given by

$$\gamma_{ij} = \eta_{ij} + 2Hl_i l_j. \quad (25)$$

as expected and the extrinsic curvature is determined from

$$K_{ij} = -\partial_t \gamma_{ij} / 2\alpha + D_i \beta_j + D_j \beta_i \quad (26)$$

$$= -\partial_t (Hl_i l_j) / \alpha + 2(D_i (Hl_t l_j) + D_j (Hl_t l_i)) \quad (27)$$

and

$$\gamma^{ij} = \delta^{ij} - 2H\delta^{il}\delta^{jk}l_l l_k / (1 + 2Hl_t^2). \quad (28)$$

Note that

$$\det \gamma_{ij} = 1 + 2Hl_t^2. \quad (29)$$

To obtain the 3-metric and extrinsic curvature we need to specify  $H$ ,  $l_\mu$ ,  $\partial_\mu H$  and  $\partial_\mu l_\nu$  and substitute these into Eq.(25) and Eq.(27). In order to evaluate  $\partial_\mu l_\nu$  and  $\partial_\mu H$  a specific choice of spacetime has to be made. For example for the Kerr spacetime we take the expressions for  $H$  and  $l_\mu$  from Eq.(12) and Eq.(11), compute their derivatives and substitute. This gives us a ‘‘Kerr-Schild’’ slice of the Kerr spacetime.

## IV. RESULTS

In the presentation that follows we first conduct a series of basic tests of the algorithm using metric and extrinsic curvature data just presented. In the second part of this section we set up a 3-dimensional Cartesian grid,  $\hat{\Sigma}$ , of  $n^3$  points, on which we define a coordinate system where the black hole (either Kerr or Schwarzschild) is placed at the origin. Using Eq.(25,27) again we generate  $\gamma_{ij}$  and  $K_{ij}$  on  $\hat{\Sigma}$  everywhere but the region that contains the curvature singularity (for Schwarzschild at

$x^2 + y^2 + z^2 = 0$  and Kerr  $\rho = \sqrt{x^2 + y^2 + z^2} \leq a$ ). With the data on  $\hat{\Sigma}$ , we start the apparent horizon locator with an initial guess surface which is a 2-sphere of radius  $r_0$ . The horizon locator surface mesh sizes used in this calculation are  $N_s = 33, 41, 49, 65, 81, 97$ . The stopping criterion for the Newton iterations was determined empirically to be  $10^{-9}$ . The cases we present are (1)  $v = 0, a = 0$  (unboosted Schwarzschild), (2)  $v = 0, a \neq 0$  (unboosted Kerr), (3)  $v \neq 0, a = 0$  (boosted Schwarzschild) and (4)  $v \neq 0, a \neq 0$  (boosted Kerr).

### A. Tests with Eddington-Finkelstein metric data

First, with  $\hat{v}_x = 0, \hat{v}_y = 0, \hat{v}_z = 0$  and  $a = 0$  (unboosted black hole in ingoing Eddington-Finkelstein coordinates) we show some basic tests of the apparent horizon locator. Most importantly we show that solutions obtained with our locator are  $O(h^2)$ . With these data all components of  $\gamma_{ij}$  and  $K_{ij}$  are non-zero. The latter property makes this a good initial model problem to work with, because the computation is fully exercised in an analytically tractable situation. As stated earlier the apparent horizon is expected to be located at  $r = 2M$ . These tests are conducted with data specified analytically where required.

#### 1. Residual Evaluation and Second Order Convergence

We place the black hole at the origin of the computational domain ( $x = 0, y = 0, z = 0$ ). In spherical symmetry for this metric the apparent horizon equation becomes the algebraic equation,

$$F(r) = \frac{1 - 2M/r}{r\sqrt{1 + 2M/r}} = 0. \quad (30)$$

A plot of  $F(r)$  is shown in FIG.(1). At  $r = 2M$  we have  $F = 0$ . A useful test of the evaluation of the expansion of the outgoing normals  $F(r)$  is to see if indeed the residual  $\hat{F}[\hat{\rho}]$  is correctly evaluated to  $O(h^2)$  as

$$\hat{F} = F + e_2 h^2 + \dots, \quad (31)$$

where  $e_2 h^2$  is the leading order truncation error term. Given that the exact value is known for  $\hat{F}[\hat{\rho}]$  we can approximate the leading order truncation error. We carry out a convergence test by evaluating  $\hat{F}[\hat{\rho}]$  on a 2-sphere of  $r = 2M$  for a series of mesh sizes,  $N_s = 17, 25, 33, 49, 65, 96, 129$ . We examined the behavior of  $\log \|\hat{F}\|_2$  (where this is the  $L_2$  norm) versus  $\log N_s$ , where  $N_s$  is the number of mesh points on one side of the  $N_s \times N_s$  mesh. At  $r = 2M$   $\hat{F} \sim e_2 h^2$  and so the  $L_2$ -norm,  $\|\hat{F}\|_2 \sim \|e_2\|_2 h^2$ . Since  $h \propto 1/N_s$  we expect that if the residual is  $O(h^2)$  then the slope of a plot of  $\log \|\hat{F}\|_2$  versus  $\log N_s$  should be  $-2.0$ , which we validated via a

least squares fit. A closely related test is to also evaluate  $\log \|\hat{\rho} - \rho\|_2$  versus  $\log N_s$ , where  $\hat{\rho}$  is the numerical solution from the apparent horizon locator and  $\rho$  is the exact horizon location. FIG.(3) shows the result. From a least squares fit to a straight line the slope is found to be  $-2.1$  which validates our solution as  $O(h^2)$ .

#### 2. Jacobian

For the same 2D mesh discussed we generate the Jacobian matrix for a single Newton step. FIG.(2) shows the structure of the matrix for a  $33 \times 33$  run. There are 1025 independent points on  $\hat{S}$  and hence  $J_{\bar{\mu}\bar{\nu}}$  is a  $1025 \times 1025$  matrix. The dots in the figure are non-zero Jacobian entries. There are seven bands in this matrix with 2 additional ones in the vicinity of the poles at  $\bar{\mu} = 1$  and  $\bar{\mu} = 1025$ . The structure reflects the domain of dependence of the finite difference operators used in the evaluation of  $\hat{F}$ . Here it comes from a combination of interpolations and Cartesian finite differencing. Near  $\bar{\mu} = 1$  and  $\bar{\mu} = 1025$  the additional bands come from our special choice of interpolation stencils at the poles, as discussed in the appendix.

The structure reflects the fact that a perturbation at a single mesh point affects the residual in a small neighborhood around it so we can optimize the generation of the Jacobian to  $O(N)$  by evaluating  $\hat{F}[\rho + \delta\rho]$  only in a small neighborhood of the perturbed point. The Jacobian generation was found to be order  $O(N^p)$  where  $p = 1.08$  and  $N$  is the total number of independent points on the 2D computational mesh.

A matrix  $A$  is defined to be diagonally dominant [15] if its elements,  $A_{ij}$ , satisfy

$$\sum_{\substack{j=1 \\ j \neq i}}^n |A_{ij}| \leq |A_{ii}| \text{ for all } i. \quad (32)$$

We found that the Jacobian is *not* diagonally dominant since the inequality in Eq.(32) is not satisfied for all  $i$  and  $j$ .

This is of interest since for some iterative solution techniques (Gauss-Seidel and SOR for example) a sufficient condition for the solution of a linear system,  $A \cdot x = b$ , is that the matrix,  $A$ , be diagonally dominant. In our case we concluded from early experiments that indeed such simple iterative solvers did not converge for this problem.

The Jacobian matrix is not symmetric but it is well-conditioned for the spacetimes that we have considered. For a  $33 \times 33$  run the Jacobian has a condition number of  $\kappa$  of about  $10^4$  to  $10^5$  where,

$$\kappa = \|A\| \|A^{-1}\|, \quad (33)$$

(In their definition of the condition number, Dongarra et al. [16] use the  $L_1$ -norm.) The condition number tells us

how close the matrix  $A$  is to being singular. A very large condition number or a reciprocal condition number close to machine epsilon tells us that  $A$  is singular. An identity matrix has a condition number of 1. To estimate  $\kappa$  we used the LINPACK library routine, DGECCO.

### 3. Solution of the Linear system

As stated before to locate the apparent horizon using our technique we have to obtain a solution,  $\delta\hat{\rho}$ , to the linear system

$$\hat{J} \cdot \delta\hat{\rho} = -\hat{F}[\hat{\rho}]$$

which is the discrete form of Eq.(8).

Since the properties of the matrix do not allow us to use the standard iterative methods such as Jacobi and Gauss-Seidel methods, We use a modified conjugate-gradient method due to Kershaw [18] (The standard form of the Conjugate gradient method will not work since  $J$  is not symmetric.) Kershaw's method, termed the Incomplete LU-Conjugate gradient method (ILUCG), can solve any linear system,  $A \cdot x = b$ , with  $A$  being any nonsingular, sparse matrix. The method involves preconditioning the matrix via an incomplete LU decomposition. This method has worked quite well for our purposes. In principle other schemes for solving the resulting system can be used.

### 4. Solution for the apparent horizon location

Using the ILUCG method to solve for  $\delta\hat{\rho}$  we demonstrate the Newton solver's ability to successfully locate apparent horizons in the Eddington-Finkelstein metric data. The apparent horizon in this data is a 2-sphere of radius  $2M$ . Using a 2-sphere of radius  $r_0$ , centered on the origin as the initial surface we carried out a series of runs for  $r_0 = 0.5..3.0$  with a  $33 \times 33$  mesh. Table (I) shows the radius,  $r_0$ , of the initial starting 2-sphere, the number of Newton iterations taken if it converged, the final residual value and the solution error. The stopping criterion is that the norm of the change in the solution,  $\|\delta\hat{\rho}\|_2$  be less than  $10^{-10}$ . We see that for all the cases, provided the solver managed to drive  $\|\delta\hat{\rho}\|_2$  below  $10^{-10}$  the final percentage error remains fixed; what differed in each case was the number of iterations taken and rate of convergence. Once the solver has driven  $\hat{\rho}$  into the vicinity of the solution the Newton convergence is quadratic. This happened in the 6th iteration in the  $r_0 = 0.5$  run. For the  $r_0 = 2.0$  run the solver took four iterations to converge down to the stopping criterion. In another series of runs with  $N_s = 33$ ,  $M = 1$  and  $r_0 = 2.5$  the perturbation parameter,  $\epsilon$ , was varied from  $10^{-1}$  to  $10^{-6}$ . An optimum value of  $\epsilon$  for this metric data was found to be about  $10^{-4}$  to  $10^{-6}$ . In general the stopping criterion need not be as stringent as we have set it. In numerical

TABLE I. This table shows a series of runs carried out for various initial conditions. The initial surface is a 2-sphere of radius  $r_0$  where  $r_0$  is shown in the first column. The number of iterations taken for the solution to achieve  $\|\delta\hat{\rho}\|_2 < 10^{-10}$  is given. Note that the final error in the solution remains a constant provided the solver is able to drive  $\|\delta\hat{\rho}\|_2$  below the specified stopping criterion. The perturbation parameter used to generate the Jacobian was  $10^{-5}$ .

$r_0$	# iterations	Final $\ \hat{F}\ _2$	$\ \hat{\rho} - \rho\ _2$	% error
0.5	10	2.2E-10	3.0E-05	1.5E-03
0.75	9	2.5E-10	3.0E-05	1.5E-03
1.00	9	9.7E-11	3.0E-05	1.5E-03
1.25	8	9.5E-11	3.0E-05	1.5E-03
1.50	7	1.6E-10	3.0E-05	1.5E-03
1.75	7	9.6E-11	3.0E-05	1.5E-03
2.00	4	9.7E-11	3.0E-05	1.5E-03
2.25	7	9.8E-11	3.0E-05	1.5E-03
2.50	8	1.0E-10	3.0E-05	1.5E-03
2.75	9	9.5E-11	3.0E-05	1.5E-03
3.00	12	9.9E-11	3.0E-05	1.5E-03

spacetimes where the metric data will have truncation error associated with them the truncation error of  $F$  is expected to be much larger than our test stopping criterion. In that case a larger stopping criterion should be chosen to avoid wasting computational effort. The optimum value is dependent on the error in the metric data. In the results we present in the paper however we drive the residuals down as far as possible. On the other hand, a perturbation parameter  $\epsilon$  must be chosen such that  $\hat{F}[\hat{\rho}+\epsilon] - \hat{F}[\hat{\rho}]$  is sufficiently large that this expression is not dominated by truncation error.

### 5. Numerical Metric data

Tests described so far used data analytically computed at each point as needed. Since the ultimate goal is to incorporate this apparent horizon location algorithm into an evolution code it is useful to gauge the performance of the algorithm with numerical metric data and with the data structures expected in the real application, where, for instance, part of the domain is excised from consideration. Thus we set up the same Eddington-Finkelstein data on a 3D Cartesian grid of  $n^3$  points, with a region of this grid excised to emulate the situation in an evolution code where the interior of the black hole is excluded. The apparent horizon surface which is embedded in this 3D Cartesian grid typically does not lie on Cartesian grid points and as a result an interpolation tool is required. If the surface mesh, during the course of the Newton iterations, overlaps the excised region then extrapolation is required. We make use of an interpolator/extrapolator written by S. Klasky [19] to obtain the 3-metric, extrinsic curvature and the spatial derivatives

of the 3-metric at any point. The use of an interpolator brings in truncation errors associated with the interpolation/extrapolation operations. In the following we show that even with extrapolation errors the solver works quite well in locating apparent horizon surfaces.

We set up a uniform 3D Cartesian grid,  $\hat{\Sigma}$ , of size  $n^3$ . On this grid we excise a region interior to a sphere of radius  $R_m$  centered at  $(x_m, y_m, z_m)$  so that the metric data is defined for  $r > R_m$  and undefined for  $r < R_m$  where  $r$  is the Cartesian distance in Kerr-Schild coordinates from the excision center.

In the following discussion on radial and offset apparent horizon locations we take  $n = 65$  for the Cartesian grid (with  $h = 1/8$ ) and  $N_s = 33$  for the surface mesh. The stopping criterion used in the horizon finder is  $\beta = 10^{-4}$ . That is, if  $\|\delta\rho\|_2 < \beta$  then the Newton iterations are stopped. The perturbation parameter,  $\epsilon$ , is taken to be  $10^{-4}$ . The interpolator tool is used to fourth order. The initial guess surface used is a sphere of radius  $r_0 = 2.1M$  centered at the origin of the Cartesian grid. With these parameters we carry out two set of tests. The first is a radial test of the horizon locator with the use of the interpolator and the second is an offset test. These tests examine the effect of extrapolation of metric data on the residual,  $\hat{F}$ , and solution to the apparent horizon equation.

#### 6. Apparent horizon location (Radial tests with excision)

In the first test case we center the black hole at  $(0, 0, 0)$ . The masked region is also centered at  $(0, 0, 0)$ . We carry out a series of tests with the excision radius,  $R_m$ , varying from 1.5 to 2.6. Thus the apparent horizon is in the defined region ( $R_m < 2M$ ) for some of the tests, and for others it is inside the excised region ( $R_m > 2M$ ). This provides evidence of the effect of extrapolations on the residual of the apparent horizon equation,  $\hat{F}$ , and the error in its solution. FIG.(4) illustrates the behaviour of the  $L_2$ -norm of the residual,  $\|\hat{F}\|_2$ , as a function of  $R_m$ . FIG.(5) shows the percentage relative error of the solution of the apparent horizon equation as a function of  $R_m$ . The percentage relative error is calculated from the exact solution for  $r = \rho(\theta, \phi) = \bar{\rho} = 2M$ . With this exact solution, we calculate the percentage relative error,  $e \equiv \|\rho - \bar{\rho}\|/\bar{\rho} \times 100\%$ . For  $R_m < 2M$  the derivative interpolator/extrapolator uses interpolation for regions near the apparent horizon location ( $r = 2M$ ), while for  $R_m > 2M$  it uses extrapolation. As  $R_m$  increases further the errors due to extrapolation increase, as expected. This can be seen in FIG.(4) where  $\|\hat{F}\|_2$  increases quickly for  $R_m \gtrsim 2.4$ , as does the error shown in FIG.(5). At  $R_m = 2.5M$ , the solver could not bring  $\|\delta\rho\|_2$  down to below  $10^{-4}$ , and so failed to meet the stopping criterion. This can be understood in terms of the Cauchy-Schwarz inequality [15], Since  $\|J \cdot \delta\rho\| = \|\hat{F}\|$  we have that

$$\|\delta\rho\| \geq \frac{\|\hat{F}\|}{\|J\|}. \quad (34)$$

At  $R_m = 2.2$  where  $\|\hat{F}\| \sim 10^{-3}$  and  $\|\delta\rho\| \sim 10^{-5}$ , we have from Eq.(34) that  $\|J\| \sim 10^2$ . Therefore at  $R_m = 2.5M$  we expect with  $\|\hat{F}\| \sim 10^{-2}$  that  $\|\delta\rho\| \sim 10^{-4}$ . By relaxing the criterion past  $R_m = 2.5$  we can still obtain a solution. Past  $R_m = 2.6$  the convergence progressively worsens. For example, at  $R_m = 2.9$ ,  $\|\hat{F}\|$  could not be brought below  $10^{-3}$ , and the solution error is 5%. The amount of error sustained from interpolation of the metric data is dependent on the resolution of the Cartesian grid and the behaviour of the functions being interpolated. If the gradients of  $\gamma_{ij}$  and  $K_{ij}$  are large near the horizon then a larger interpolation error is sustained. This in turn leads to a larger truncation error in  $F$ . In the numerical evolution of black hole spacetimes with excision then buffer zones may not be necessary for the location of apparent horizons. However, for other reasons buffer zones might be necessary.

#### 7. Locating Offset apparent horizons

We examine behaviour of the locator with the derivative interpolator for a black hole offset so that it overlaps the excised region. This is important in tracking moving black holes [20].

The center of the masked region is at  $(0, 0, 0)$  and the black hole of radius  $2M$  is centered at  $(\delta/\sqrt{3}, \delta/\sqrt{3}, \delta/\sqrt{3})$ , so that the radial distance between the mask center and the hole is  $\delta$ . With a grid spacing of  $h = 1/8$ , an offset of  $\delta = 1$  corresponds to approximately 8 grid zones. FIG.(6) shows the percentage relative error in the apparent horizon location as a function of the offset  $\delta$ . As the graph illustrates, up to  $\delta = 0.7$  the percentage relative error is below one percent. (At  $\delta = 0.7$  the percentage error is 0.6%.) From  $\delta = 0.7$  onwards, however the solver becomes sensitive to initial conditions and extrapolation errors and quickly ceases to converge.

At  $\delta = 0.7$ , about 5-6 grid points offset, we are still able to find horizons. Generally in explicit time-evolution codes the CFL condition [22] restricts the black hole motion from one time slice to another, to be less than one zone ( $\delta < h$  or about  $\delta \sim 0.1$  in our test case). Hence we expect, based on the results for our model spacetime as shown in FIG.(6), that in such an evolutionary scheme with a similar resolution we will be able to track black hole apparent horizons to less than 0.1%.

#### B. Apparent Horizons in Boosted Kerr data

In this section we now focus on apparent horizon location for boosted Kerr and Schwarzschild black holes. For the data that follow we excise a 2-sphere of radius  $r > a$

centered about the origin from the computational domain to avoid the ring singularity structure of the Kerr black hole. Using the interpolator tool in conjunction with the apparent horizon locator, we locate horizons for various values of the angular momentum parameter,  $a$ . The horizon locator begins with a trial surface which is a 2-sphere of radius  $r_0 = 2M$ . The locator was run for  $a = 0.0, 0.1, 0.2, \dots, 0.9$  at  $N_s = 33$ . FIG.(7) shows a cross-section of the horizon in the  $xz$  plane as a function of  $a$ . The apparent horizon is seen to have the shape of an oblate spheroid. In the runs used to generate these data we used  $\epsilon = 10^{-5}$  and a stopping criterion that ensured that the  $l_2$ -norm of  $\hat{F}$  on the computational mesh was less than  $10^{-11}$ .

FIG.(8) shows the  $l_2$ -norm of the error in the solution,  $\|(\hat{r} - r_+)/r_+\|_2$ , versus mesh size. This set of runs was carried out with  $a = 0.9$  and  $N_s = 17, 25, 33, 49, 65$ . Where  $r_+$  is given by (17) and the  $\hat{r}$  is computed from

$$\hat{r} \equiv \left\{ \frac{1}{2} (\hat{\rho}^2 - a^2) + \left[ \frac{1}{4} (\hat{\rho}^2 - a^2)^2 + a^2 z^2 \right]^{1/2} \right\}^{1/2} \quad (35)$$

where  $\hat{\rho} = \sqrt{x^2 + y^2 + z^2}$  is the solution from the apparent horizon locator. From a least squares fit the slope is found to be  $-2.1$  and the solution is  $O(h^2)$ .

The area of the event horizon in the Kerr spacetime [23] is given by

$$\mathcal{A} = 4\pi (r_+^2 + a^2) \quad (36)$$

Let  $\hat{\mathcal{A}}$  be the computed apparent horizon area. FIG.(9) shows the percentage errors  $\|(\hat{\mathcal{A}} - \mathcal{A})/\mathcal{A} \times 100\%\|_2$  versus  $a$  for various resolutions  $N_s = 17, \dots, 65$ . The area of the apparent horizon is computed via a technique which projects the 3-metric,  $\gamma_{ij}$ , onto the 2-surface to obtain an area element  $\sqrt{^{(2)}\gamma} d\theta d\phi$ , and then computes the surface integral. FIG.(9) shows the percentage errors in the area for increasing resolution. We now consider Schwarzschild and Kerr black holes boosted in the  $yz$ -direction. That is, we look at  $\hat{v}_x = 0, \hat{v}_y = 1/\sqrt{2}, \hat{v}_z = 1/\sqrt{2}$  and  $a = 0, 0.9$ . In each of these cases we locate apparent horizons for  $v = 0, 0.1, \dots, 0.9$ . From  $v = 0$  to  $v = 0.8$  we started with a two-sphere of radius  $2M$  and found an apparent horizon with outgoing expansions driven down to  $10^{-12}$ . For  $v > 0.8$  we had difficulty driving the expansions down. As a result we utilized the solution at  $v = 0.8$  as an initial guess and were subsequently able to find horizons by stepping every 0.25 from  $v = 0.8$  to  $v = 0.9$ . We used  $\epsilon = 10^{-5}$  again for these runs. At  $v = 0$  the initial guess is the apparent horizon and there within the six Newton iterations the expansions were driven down around  $10^{-12}$ . The first Newton iteration took the expansions down around  $10^{-6}$ . For  $v = 0.5$  starting from an initial guess of a sphere of radius  $\rho = 2M$  it took four Newton iterations to drive the expansions down around  $10^{-6}$  and nine Newton iterations to get down to  $10^{-12}$ . Typically in a numerical time-evolution of such a spacetime we would

not need to drive the expansions down to this level. If we are utilizing a surface within the apparent horizon as an excision boundary then we need only to drive the expansions down far enough to be certain an apparent horizon is present. FIG.(10) shows the  $yz$ -cross-section of the apparent horizon for various boost velocities compared against an unboosted black hole apparent horizon cross-section. We find that the apparent horizon is Lorentz contracted in the  $yz$ -direction in the boosted coordinates. We have considered a slice of such a boosted spacetime in which the event horizon appears Lorentz contracted in the resulting coordinates. We know that in these spacetimes the apparent horizon should coincide with the event horizon and we find that this is indeed the case. First, the area of the apparent horizon coincides with the area of the event horizon which is invariant under a boost. FIG.(11) shows the error in the apparent horizon area as a function of  $v$  for various resolutions. We find that with increasing resolution the error in the area converges towards zero. This demonstrates that the area of the apparent horizon is invariant under a Lorentz boost. This is coupled to an interesting property of the Kerr-Schild type of metrics that  $r = r_+$  remains fixed for Kerr and Schwarzschild black holes. This is illustrated in FIG.(12) where we show the error in the radial coordinate  $r = 2M$  on the apparent horizon for various boost velocities. In this case the black hole is boosted in the  $xyz$ -direction for generality. That is,  $\hat{v}_x = 1/\sqrt{3}, \hat{v}_y = 1/\sqrt{3}, \hat{v}_z = 1/\sqrt{3}$  and  $a = 0$ . Here  $r$  is computed from the boosted coordinates. We find that  $r$  converges towards  $2M$  for increasing resolution satisfying yet another property of the boosted Kerr-Schild spacetime.

FIG.(13) shows surface plots of the apparent horizon for  $v = 0, 0.3, 0.6$  and  $v = 0.9$  displayed in Kerr-Schild Cartesian coordinates. Note how distorted the apparent horizon gets with increasing boost velocities. As seen in the figures for the  $yz$ -boosts the boosted apparent horizons in this case are always contained within the apparent horizon for  $v = 0$ . That is, the boost contracts the apparent horizon in the boost-direction. Again for a boost velocity of  $v = 0.5$  it took the solver eight Newton steps to drive the expansions down around  $10^{-12}$ . The stopping criterion used in this run was  $10^{-12}$  and the final expansions are  $\sim 10^{-13}$ . On average it took four Newton steps to drive the expansions down to  $\sim 10^{-6}$  and nine Newton steps to  $\sim 10^{-12}$  starting from an expansion of 0.1.

In the case of a boosted Kerr black hole with  $a = 0.9$  the results are again very similar to those of the Schwarzschild black hole. Note that now with  $a = 0.9$  and  $v \rightarrow 0.9$  we get even more distorted apparent horizons. These results show that this algorithm for finding apparent horizons does quite well with such large distortions. In addition the cost of finding these surfaces increases by only two additional Newton steps. FIG.(14) shows the  $yz$ -cross-sections for the apparent horizon found for  $a = 0.9$  as a function of  $v$ . Again the boosted apparent horizon is contained within the un-



boosted one and Lorentz contracted. FIG.(15) shows the error in the area for the same data. With  $a = 0.9$  we expect that the area should be  $\sim 36$ . The graph shows that for increasing resolution the error in the area tends towards zero. Hence the area remains fixed with increased boost velocity as is expected.

Similarly,  $r$  computed from the boosted coordinates remains fixed at  $r_+$  as is shown by FIG.(16). The apparent horizons found here were obtained with  $\hat{v}_x = 1/\sqrt{3}$ ,  $\hat{v}_y = 1/\sqrt{3}$ ,  $\hat{v}_z = 1/\sqrt{3}$  and  $a = 0.9$ . That is, the boost was in the  $xyz$ -direction with magnitude  $v$ . Again we find that  $r$  on the apparent horizon converges to  $r_+ \sim 1.4$  with increasing resolution for all boost velocities. At a resolution of  $33 \times 33$  we have an percentage error of 8% and 1% at  $65 \times 65$ . FIG.(17) shows surface plots of the apparent horizon for the boosted Kerr black hole for  $v = 0, 0.3, 0.6$  and  $0.9$ . Note how distorted the final apparent horizon surface is. Our algorithm required one more Newton step to drive the expansions down to  $10^{-13}$  for  $v = 0$  compared to  $v = 0.9$ . It took six Newton iterations to drive the resolution from about 0.2 at the initial step to  $10^{-6}$  for both boost velocities. Hence, this algorithm has the advantage that given sufficient resolution on the computational mesh, the work done does not drastically increase for increasing distortions.

## V. DISCUSSION

We have demonstrated in this paper that our method based on finite difference techniques is viable for locating very distorted boosted Kerr black hole apparent horizons. We have shown that the located horizons obey the expected analytical rule, of invariance of the area of the event horizon, in cases corresponding to at-rest or boosted single black holes, where the apparent horizon is known to coincide with the event horizon. We have additionally given a number of computational tests demonstrating the behavior of the tracker on interpolated or extrapolated data which is realistically similar to that from evolutions. In other contexts algorithm has been thoroughly tested with the canonical set of test problems such as the two and three black hole initial data sets and additionally in an evolution code tracking the apparent horizon for a Schwarzschild black hole in geodesic slicing [21] and demonstrated to be capable of tracking apparent horizons in boosted Schwarzschild data [20]. Those tests and the tests given here show its viability as a method for locating black hole apparent horizons and using them for black hole excision. Since black hole excision is essential for long-term evolutions of single or multiple black hole spacetimes. It is very useful to have efficient apparent horizon locators that can locate apparent horizons “fast” relative to the time taken for an evolution time step.

Our algorithm is dominated primarily by computations of the Jacobian matrix in the use of Newton’s method. These operations are optimized such that they scale as

$\mathcal{O}(N)$  approximately where  $N$  is the total number of points on the two-dimensional mesh used for the solution. With a  $33 \times 33$  mesh we find that each Newton iteration takes on average 20 Origin 2000 CPU seconds. This is independent of the distortion of the apparent horizon. However the number of Newton iteration steps is determined by the “distance” of the initial starting surface from the final solution. During the course of an evolution it is expected that the apparent horizons over several timeslices will be “close” enough to each other that two to three Newton iterations will be sufficient to locate the horizon at low accuracy with the expansion of the outgoing null rays on its surface being at the level of  $10^{-5}$  or  $10^{-6}$ . Obtaining a better accuracy requires more Newton iterations and the number of timesteps taken depends also on the accuracy of the background metric data. Typically in our model problems eight iterations will take us below  $10^{-10}$ .

One of the drawbacks of a Newton’s method for finding apparent horizons is its sensitivity to the initial guess. An initial guess outside of the radius of convergence will not lead to a solution. Additionally Newton methods are known to be sensitive to high frequency components in the solution. This is demonstrated in axisymmetry by Thornburg [8]. Sensitivity to the initial guess can be easily handled by combining the Newton method algorithm with apparent horizon trackers that are based on flow methods. The flow finder is used to obtain an initial guess for the Newton method which then converges on the solution very quickly.

The efficiency of our boundary-value method can be compared to the efficiency of other approaches (variations of flow methods) due to Tod, as developed by Shoemaker et al. [12] and fast flow methods developed by Gundlach [13]. The flow method is based on a parabolic partial differential equation whose rate of convergence to the solution slows as it approaches it. Typically for a  $33 \times 33$  run the flow method takes on the order of thousands of seconds to converge down to expansions of  $10^{-4}$ . The advantage of this method however is its ability to find multiple apparent horizons from an arbitrary initial guess. Combined with the Newton finder this will result in a robust apparent horizon finding scheme.

We can also compare the effort to spectral decomposition methods. We concentrate on a method similar to that of Nakamura et al. [4] in which the equation for the apparent horizon surface is written:

$$\rho(\theta, \phi) = \sum_{l=0}^{l_{max}} \sum_{m=-l}^l a_{lm} Y_{lm}(\theta, \phi). \quad (37)$$

We do not have access to an apparent horizon finder based on pseudo-spectral methods but we will analytically compute the coefficients for the case of a boosted Schwarzschild black hole; this will give some insight into the range of harmonics required, and some idea of what scaling of these methods might be.

In Kerr Schild coordinates, the hole, with boost in the z-direction, has the shape of a spheroid,

$$\frac{x^2}{a^2} + \frac{z^2}{b^2} = 1, \quad (38)$$

where we have suppressed the y-direction.

Notice that the axes  $a, b$  of the ellipsoid obey  $b^2/a^2 = 1 - v^2$ , which demonstrates that the eccentricity is directly proportional to the boost velocity,  $\epsilon = v$ , for this case. Hence even ellipses with moderate ratio of axes, such as that for  $v=0.9$ , where the ratio is a little less than 0.5, have moderately large eccentricities. We will approximate the form Eq.(38) with an axisymmetric series of the form Eq.(37) (the general case would have nonaxisymmetric terms also). We find it more convenient to work with Legendre polynomials than with the spherical harmonics directly.

Since we work with Legendre polynomials, we drop the y- coordinate in the spheroid expression, to obtain :

$$R(\theta) = b/\sqrt{1 - \epsilon^2 \sin^2 \theta} \quad (39)$$

$$= b/\sqrt{1 - \epsilon^2(1 - q^2)}, \quad (40)$$

where  $q = \cos \theta$ .

To obtain the expansion of expression Eq.(40) in terms of  $P_m$ , we first expand using the binomial theorem.

$$R(\theta)/b = \sum_{s=0}^{\infty} \binom{-1/2}{s} (-1)^s \epsilon^{2s} (1 - q^2)^s. \quad (41)$$

This converges for all  $v < 1$ .

Using the binomial theorem again for  $(1 - q^2)^s$  we substitute

$$(1 - q^2)^s = \sum_{r=0}^s \binom{s}{r} (-1)^r q^{2r} \quad (42)$$

in (41) to obtain

$$R(\theta)/b = \sum_{s=0}^{\infty} \binom{-1/2}{s} (-1)^s \epsilon^{2s} \sum_{r=0}^s \binom{s}{r} (-1)^r a_{sr} \quad (43)$$

where

$$a_{sr}(q) = \sum_{n=0}^r \frac{2^{2n}(4n+1)(2r)!(r+n)!}{(2r+2n+1)!(r-n)!} P_{2n}(q) \quad (44)$$

and we made the substitution

$$q^{2r} = \sum_{n=0}^r \frac{2^{2n}(4n+1)(2r)!(r+n)!}{(2r+2n+1)!(r-n)!} P_{2n}(q).$$

By exchanging the summations over  $r$  and  $n$  and then  $n$  and  $s$  it is possible to rewrite Eq.(43) as

$$r(\theta) = \sum_{n=0}^{\infty} C_{2n} P_{2n}(\theta), \quad (45)$$

where

$$C_{2n} = 2^{2n}(4n+1) \sum_{s=n}^{\infty} \binom{-1/2}{s} (-1)^s \epsilon^{2s} \times \sum_{r=n}^s \binom{s}{r} \frac{(-1)^r (2r)!(r+n)!}{(2r+2n+1)!(r-n)!}. \quad (46)$$

FIG.(18) gives the coefficients  $C_{2n}$  for  $n = 1, \dots, 10$ , and for several values of  $v$ . While FIG.(18) shows the exponential convergence of algorithm with  $n$ , it also shows that the coefficient of the convergence is small for  $v \sim 0.9$ . It can be seen that the number of required terms approaches 20 for  $v = 0.9$  if the error is required to be less than  $10^{-3}$ . (The general sum would have polynomials of odd as well as even order, and for each  $l$ , a set of azimuthal quantum numbers spanning  $-2n$  to  $2n$ ). Hence in general, to compute the distorted apparent horizon would take a search over  $20^2$  parameters in a minimization routine. This is equivalent to inverting a full matrix of this size, and would be expected to be slow. The boundary value problem is expected to be much faster. It is a fact that the boundary value problem as now implemented does not handle multiple black-hole spaces, so its speed is counteracted by the impossibility of using it in 2-hole cases. However, it may be possible to use a flow method which does recognize the existence of separate black holes, run down to find the two holes each with some accuracy, and then to use this boundary solution code to quickly get a highly accurate result. We are confident such a combined tool would be of great utility.

## VI. ACKNOWLEDGEMENTS

We wish to thank S.Klasky for providing and developing the 3d interpolation tools used in a part of this work as well as for discussions and work on applications of interpolation with excision. MFH wishes to thank J.Thornburg for stimulating discussions on apparent horizon location during the early part of this work. This work was supported by NSF PHY9800722 and PHY9800725 and PHY9800970.

- 
- [1] J.W. York in *Frontiers in Numerical Relativity*, ed. C.R. Evans, L.S. Finn and D.W. Hobill (Cambridge Univ. Press, 1989)
  - [2] Hawking, S. and Ellis, G.: "The Large Scale Structure of Space-Time", Cambridge University Press, Cambridge (UK), 1973.
  - [3] R. Wald and V. Iyer, Phys. Rev. D **44**, R3719-R3722 (1991).
  - [4] T. Nakamura, Y. Kojima, and K. Oohara, Phys. Lett., **106A**, 235-239, (1984).

- [5] N.T. Bishop, *General Relativity and Gravitation*, **14**, No. 9, 1982.
- [6] P. Anninos, K. Camarda, J. Libson, J. Masso, E. Seidel and W.-M. Suen, *Phys. Rev. D* **58** 024003 (1998).
- [7] T. Baumgarte, G.B. Cook, M.A. Scheel, S.L. Shapiro, and S.A. Teukolsky, "Implementing an Apparent Horizon Finder in Three-dimensions", *Phys. Rev. D* **54** 4849-4857 (1996).
- [8] J. Thornburg, "Finding apparent horizons in numerical relativity", *Phys Rev D.*, **54**, 4899-4918 (1996).
- [9] K.P. Tod, *Class. Quantum Grav.* **8**, L115-L118 (1991).
- [10] D.H. Bernstein, "Notes on the mean curvature flow method for finding apparent horizons", Unpublished notes.
- [11] E. Pasch, *SFB 382 Report Number* **63** (1997).
- [12] D. Shoemaker, M.F. Huq and R.A. Matzner, *in preparation*.
- [13] C. Gundlach, "Pseudospectral apparent horizon finders: An efficient new algorithm", *Phys Rev D* **57** R863 (1998).
- [14] M.W. Choptuik, "A Study of Numerical Techniques for Radiative Problems in General Relativity", Ph.D dissertation, The University of British Columbia, July 1986.
- [15] Ortega, J. and Rheinboldt, W., "Iterative Solution of Nonlinear Equations in Several Variables", Academic Press, Inc., (USA) 1970.
- [16] J.J. Dongarra, J.R. Bunch, C.B. Moler and G.W. Stewart, "LINPACK : Users' Guide", Philadelphia : Society for Industrial and Applied Mathematics, 1978.
- [17] Personal Communication
- [18] D. S. Kershaw, *Journal of Comp. Phys.*, **26**, 43-65 (1978).
- [19] S. Klasky, M. Choptuik and R. Matzner, "Interpolators/Extrapolators for AMR Finite Difference codes", Technical Report, Center for Relativity, University of Texas at Austin (1995).
- [20] M.F. Huq, Third Texas Workshop on 3-dimensional Numerical Relativity, The University of Texas at Austin, October 30th to November 1st 1995.
- [21] M.F. Huq, "Apparent Horizon Location in Numerical Spacetimes", Ph.D dissertation, The University of Texas at Austin, December 1996.
- [22] R. Courant, K.O. Friedrichs, and H. Lewy, English Translation of "Über die Partiellen Differenzgleichungen der Mathematischen Physik", *Math. Ann.* 100, 32-74 (1928), *IBM Journal*, **11**(2) 215-238, (March 1967).
- [23] C.W. Misner, K.S. Thorne and J.A. Wheeler, "Gravitation", W.H. Freeman and Company, New York (1973).

## VII. APPENDIX A: EVALUATION OF THE RESIDUAL

The evaluation of Cartesian derivatives on  $\hat{\mathcal{S}}$  is carried out by constructing 3D finite difference stencils at each mesh point on  $\hat{\mathcal{S}}$ . The finite difference stencil, denoted by  $\mathcal{N}$ , consists of 26 additional points around each mesh point. These 26 points are  $\pm\delta x$ ,  $\pm\delta y$  and  $\pm\delta z$  away from the central mesh point as shown in FIG.(19). These points, as shown, are organized into three planes of constant  $z$ :  $z = z_0 - \delta z$ ,  $z_0$ ,  $z_0 + \delta z$ . Each plane contains the nine nearest neighbors to the center point, including the center point itself in the case of  $z = z_0$ . We use a single discretization scale  $h$  ( $\delta x = \delta y = \delta z = h$ ) which is always proportional to the mesh spacing  $\delta\theta = \pi/(N_s - 1)$ .

To define  $\varphi(x, y, z)$  at each stencil point  $\mathbf{x} \in \mathcal{N}$  we use its split into radial and angular parts,  $\varphi(x, y, z) = r - \rho(\theta, \phi)$ . For each stencil point  $\mathbf{x}$  we compute the corresponding spherical coordinates  $(r_x, \theta_x, \phi_x)$ . This point can be thought of as a ray emanating from the origin of our spherical coordinate system (which coincides with the origin of our Cartesian coordinate system) along  $(\theta_x, \phi_x)$  of length  $r_x$ . FIG.(20) labels the point  $\mathbf{x}$  as P. The dashed line from P to the origin is the ray from the origin. Its intersection with  $\hat{\mathcal{S}}$  is denoted by a filled square. The value of  $\varphi$  at  $\mathbf{x}$  can be obtained by computing  $\rho(\theta_x, \phi_x)$  via bi-quartic interpolation where the truncation error has a leading order term which is fourth order in the grid spacing  $h$ . The interpolation is carried out with values of  $\hat{\rho}$  defined on mesh points of  $\hat{\mathcal{S}}$  using a 16 point stencil. FIG.(21) shows the choice of these stencil points in the interior of the mesh. At the poles a special choice is made of stencil points which takes into account the indentifications made at the poles. FIG.(22) shows a choice of stencil points for an interpolation point near the pole. This approach leads to a fourth order truncation error in  $\rho(\theta_x, \phi_x)$  at all points on  $\hat{\mathcal{S}}$ . Then  $\varphi$  can be constructed for every  $\mathbf{x} \in \mathcal{N}$  as  $\varphi = r_x - \rho(\theta_x, \phi_x)$ . Using this approach  $\varphi$  is defined at any finite difference stencil point for every mesh point on  $\hat{\mathcal{S}}$ . The finite difference expressions for  $\Delta_i^h \varphi$ ,  $\Delta_i^h \Delta_j^h \varphi$  (corresponding to first and second derivatives) are computed at each of the mesh points. The residual is then evaluated on  $\hat{\mathcal{S}}$  using these finite difference approximations for the derivatives to  $O(h^2)$ , and metric data  $(\gamma_{ij}, \partial_k \gamma_{ij}, K_{ij})$  which are specified either analytically or interpolated from an enveloping 3D Cartesian grid.

Because we use  $O(h^2)$  finite difference approximations  $\Delta_i^h \varphi$ ,  $\Delta_i^h \Delta_j^h \varphi$  to the derivatives, this approach leads to an  $O(h^2)$  truncation error in evaluating  $\hat{F}[\hat{\rho}]$ . Because of our special attention to points near the pole,  $\hat{F}$  is evaluated smoothly everywhere on  $\hat{\mathcal{S}}$ .

With a means for evaluating  $\hat{F}$  at any point in the domain of  $\hat{\mathcal{S}}$  it is straightforward to generate  $\hat{J}_{\bar{\mu}\bar{\nu}}$  numerically using Eq.(9). The algorithm for this is summarized as follows:

Specify metric data everywhere on  $\hat{\mathcal{S}}$

Evaluate  $\hat{F}[\rho]$  everywhere on  $\hat{\mathcal{S}}$   
 For each point (labelled by  $\bar{\nu}$ ) in  $\hat{\mathcal{S}}$   
   Perturb  $\rho_{\bar{\nu}} = \rho_{\bar{\nu}} + \epsilon$   
   Specify metric data on perturbed point  
   Evaluate  $\hat{F}[\rho_{\bar{\nu}} + \epsilon]$  at the  $\bar{\mu}$ -th point.  
   Compute the  $\bar{\mu}\bar{\nu}$  component of the Jacobian matrix  
   using (9)  
 End loop over points on  $\hat{\mathcal{S}}$ .

This gives the Jacobian matrix,  $\hat{J}_{\bar{\mu}\bar{\nu}}$ , for  $\hat{F}$  evaluated.  
 $\hat{J}_{\bar{\mu}\bar{\nu}}$  is a  $(N_s^2 - 2N_s + 2) \times (N_s^2 - 2N_s + 2)$  matrix which  
 is used in Newton's method as follows:

Start with an initial guess surface  $\hat{\rho} = \hat{\rho}_0$   
 while  $\|\hat{F}\| > \text{stopping criterion}$   
   Compute the Jacobian  $\hat{J}_{\bar{\mu}\bar{\nu}}$  for the current  $\hat{\rho}$   
   Evaluate  $\hat{F}[\hat{\rho}]$   
   Solve  $\hat{J} \cdot \delta\hat{\rho} = -\hat{F}[\hat{\rho}]$  for  $\delta\hat{\rho}$   
   Update the surface  $\hat{\rho} = \hat{\rho} + \delta\hat{\rho}$

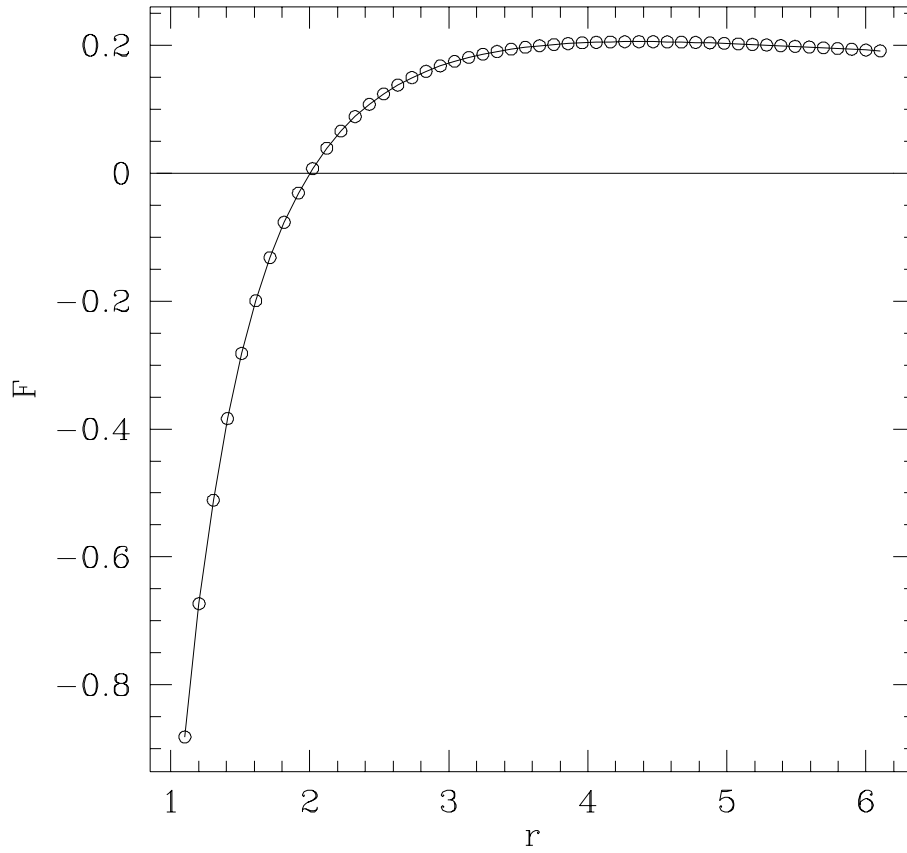


FIG. 1. Figure showing the value of  $F$ , given by eqn(30), is shown as a function of  $r$ .  $F(r)$ , is evaluated on a series of 2-spheres of radius  $r_0$ . At  $r = 2M$   $F = 0$  and as  $r \rightarrow \infty$ ,  $F \rightarrow 0$ . As  $r \rightarrow 0$ ,  $F \rightarrow -\infty$ . The maximum value of  $F$  is  $0.206/M$  at  $r = 4.372M$

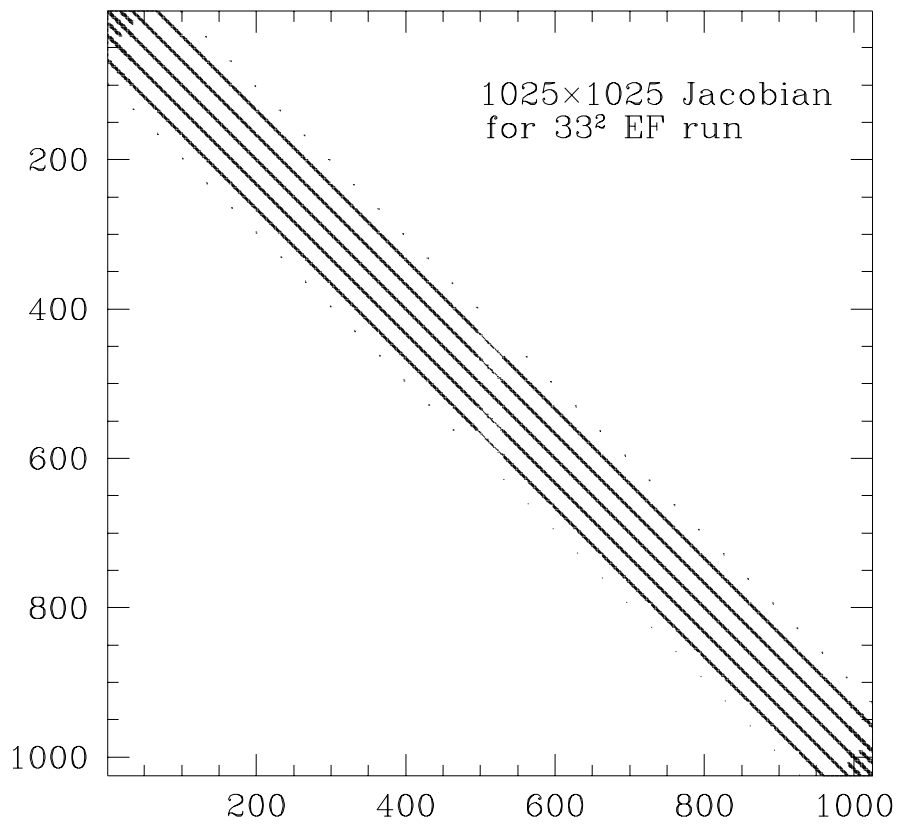


FIG. 2. This figure shows the sparsity structure of the Jacobian matrix for a  $33 \times 33$  run.

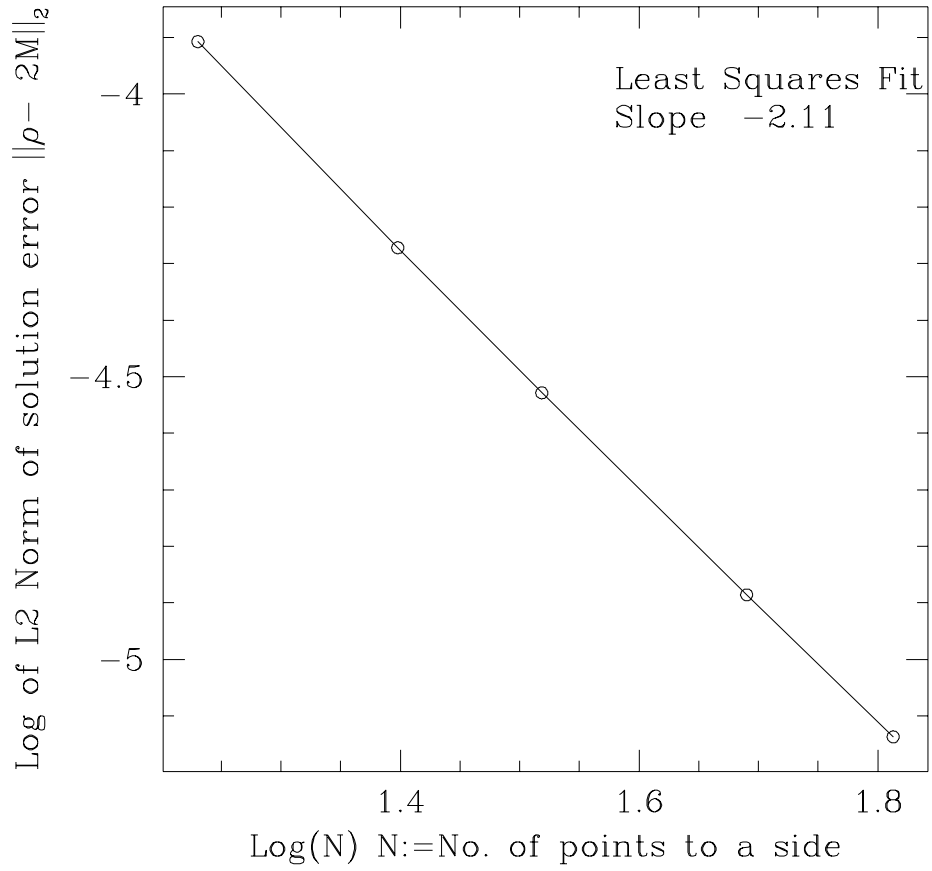


FIG. 3. This graph shows the log of the error norm of the numerical solution,  $\|\hat{\rho} - \rho\|_2$  versus  $\log(N_s)$ . The slope of the graph is  $-2.11$  and hence the solution is  $O(h^2)$ .

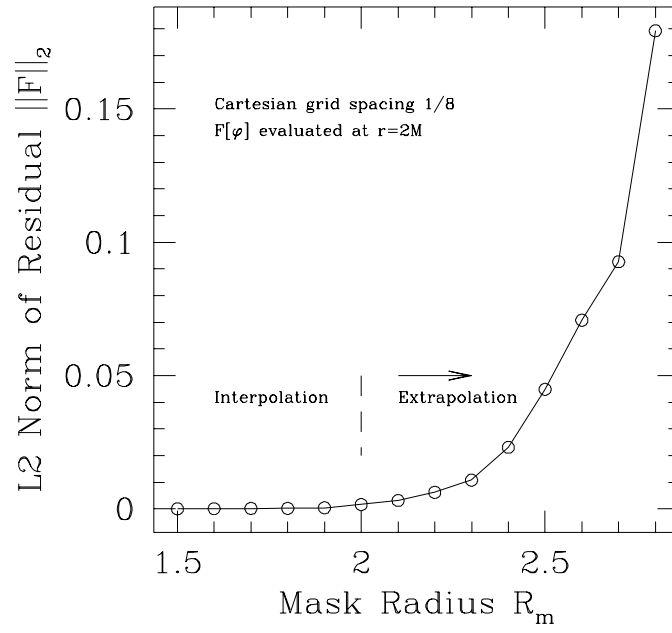


FIG. 4. Graph of the  $L_2$ -norms of the residual,  $\|\hat{F}[\varphi]\|$ , versus the mask radius,  $R_m$



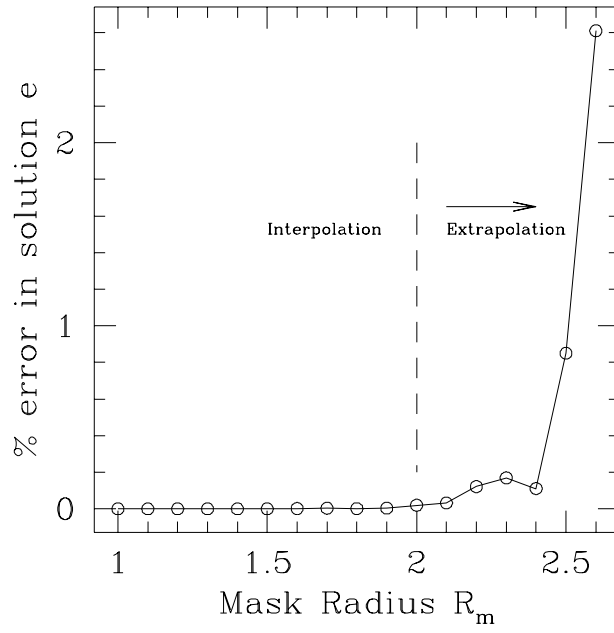


FIG. 5. Graph of percentage relative error in  $\rho$  versus mask radius. Note that past  $R_m = 2.5$  the solver did not meet the stopping criterion of  $10^{-4}$ .

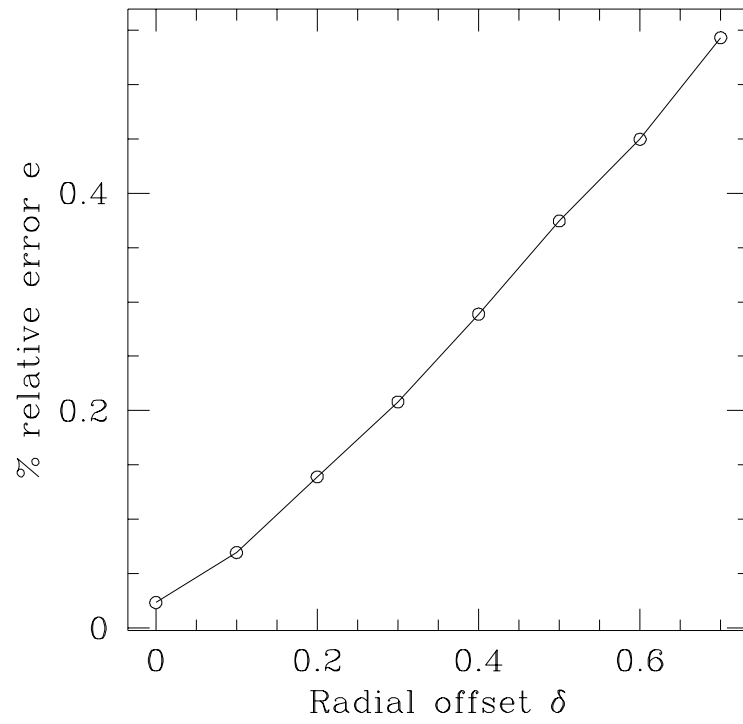


FIG. 6. Percentage relative error as a function of the offset  $\delta$ .

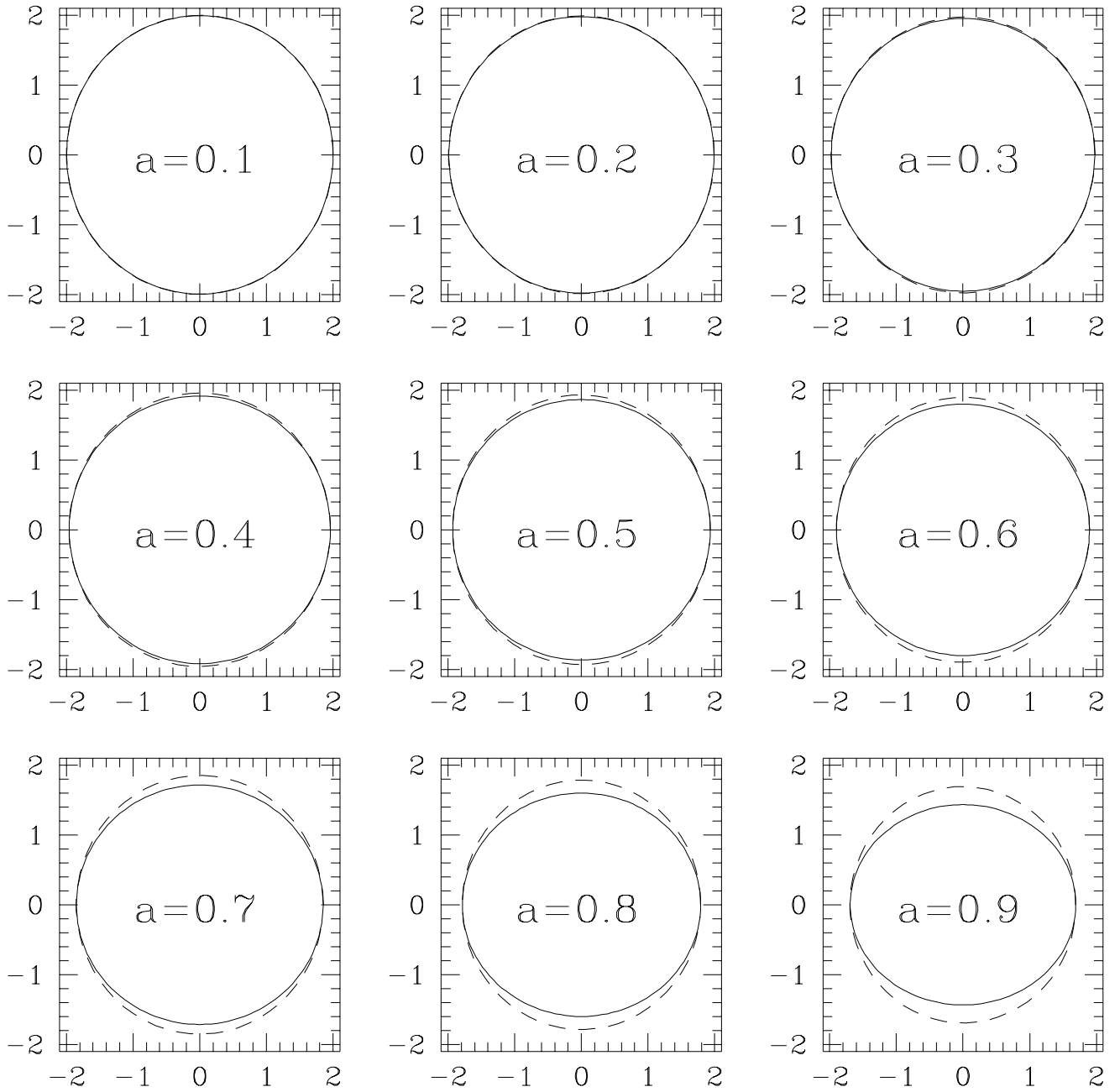


FIG. 7. The following figure shows the cross-section of apparent horizons located for various values of  $a$ . The solid line shows the  $\phi = \pi$  slice of the apparent horizon. The dashed line shows the  $\theta = \pi/2$  slice of the horizon. As expected the  $\phi = \pi$  slices show increasing deformation for increasing  $a$ .

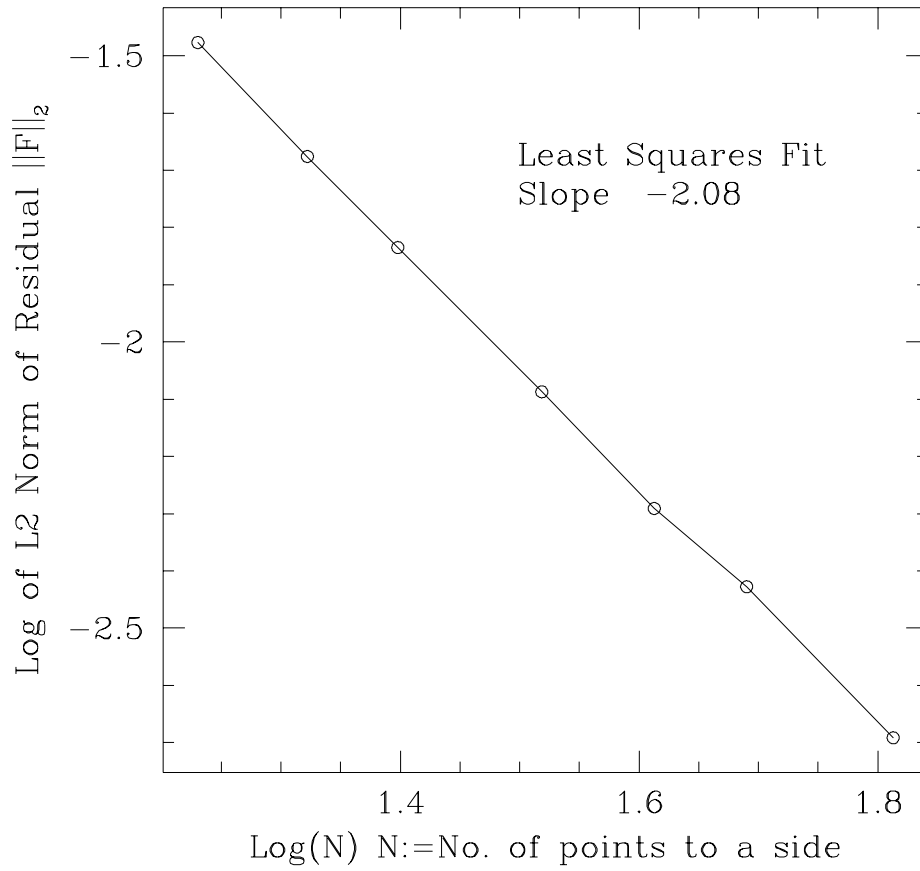


FIG. 8.  $\|\hat{r} - r_+\|_2$  versus  $N_s$  for  $a = 0.9$ .

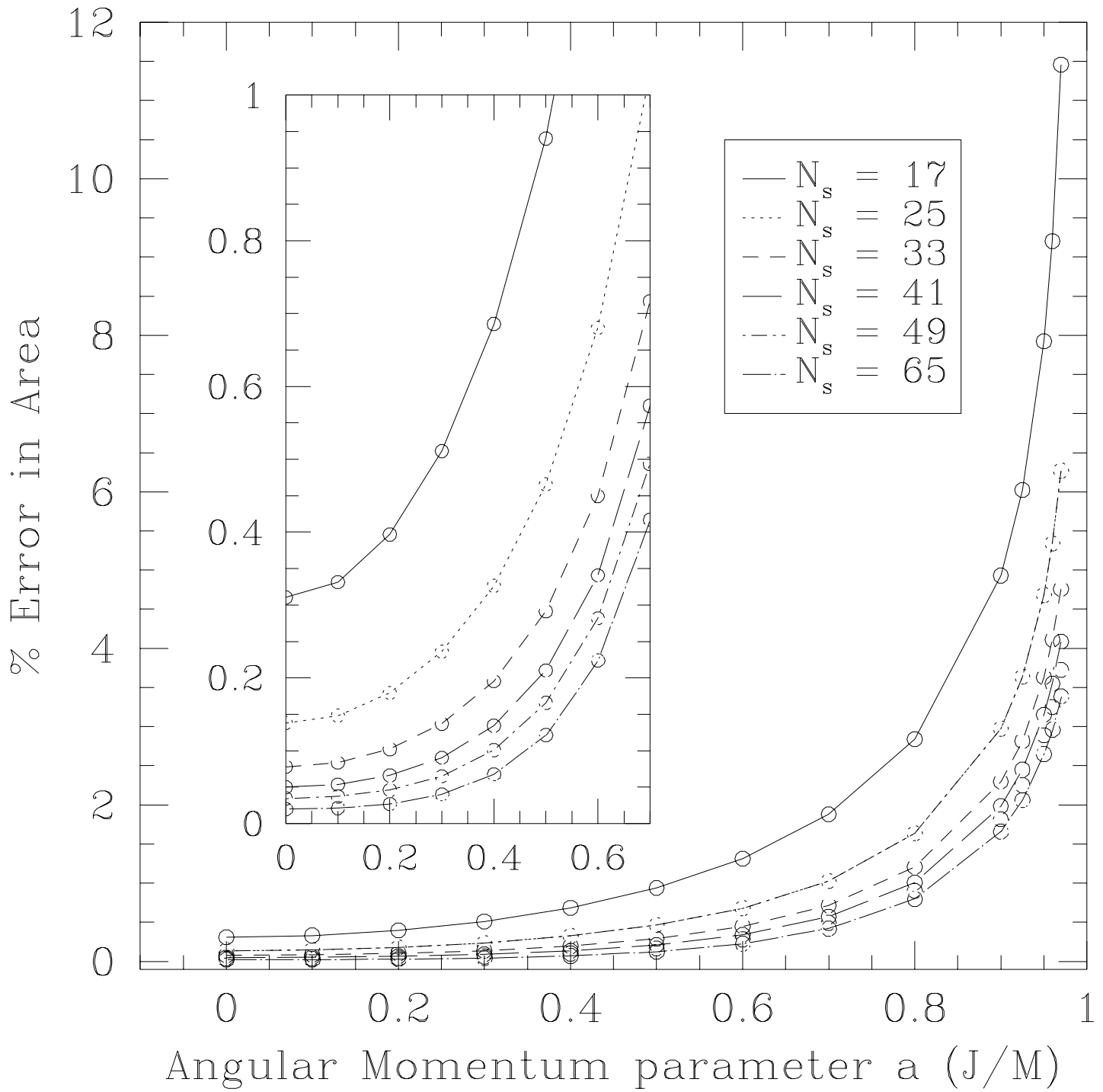


FIG. 9. The percentage error in the area of the apparent horizon for a Kerr hole versus  $a$  is shown for  $N_s = 17, 25, 33, 41, 49, 65$ .

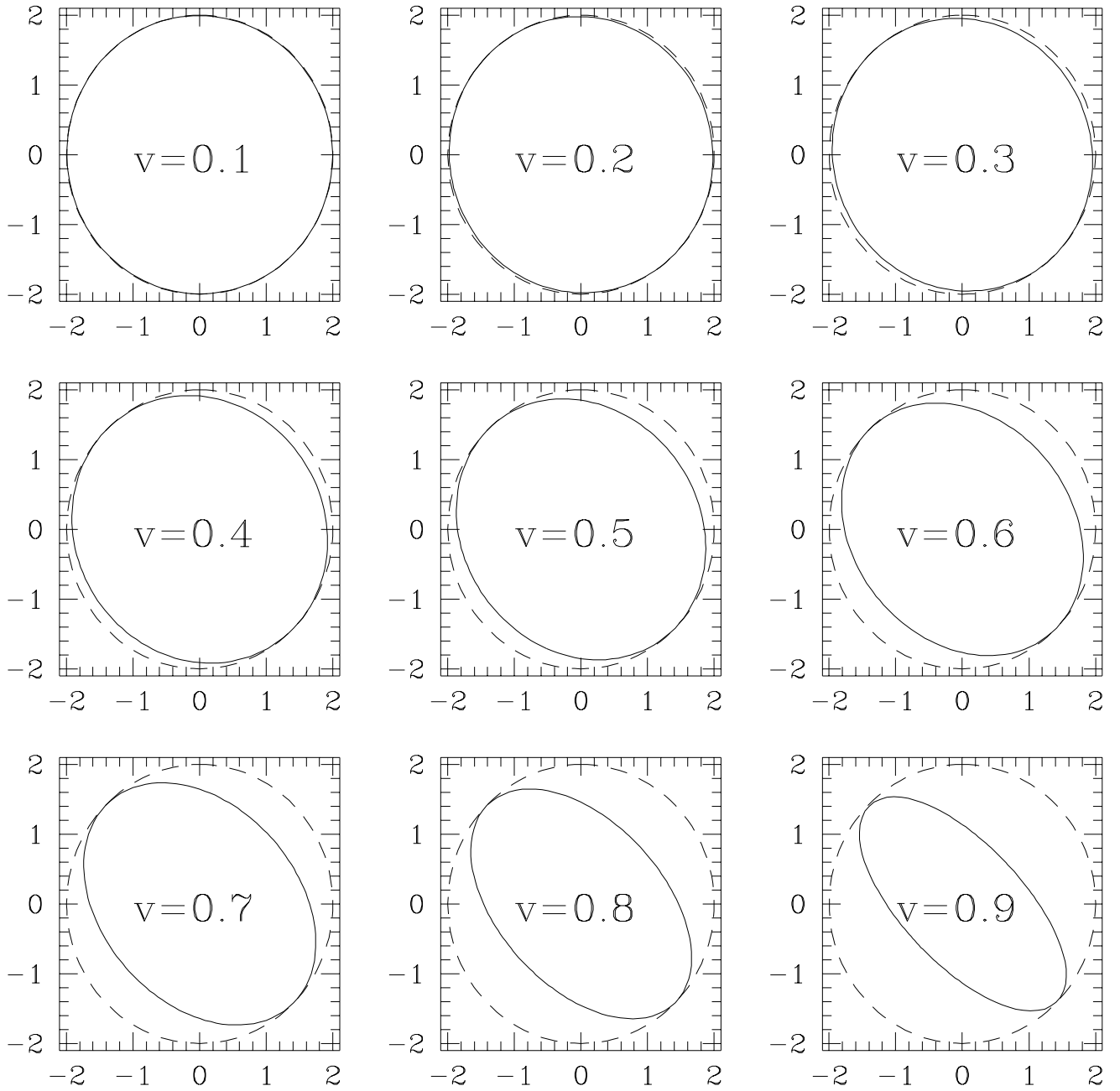


FIG. 10. This figure shows the y-z cross-section of Schwarzschild black hole apparent horizons located for boost velocities of  $v = 0.0, 0.1, \dots, 0.9$  in the y-z direction. The dashed circle in each of these figures is the apparent horizon for an unboosted Schwarzschild black hole. Note that the point of contact is along the y-z direction orthogonal to the direction of the boost.

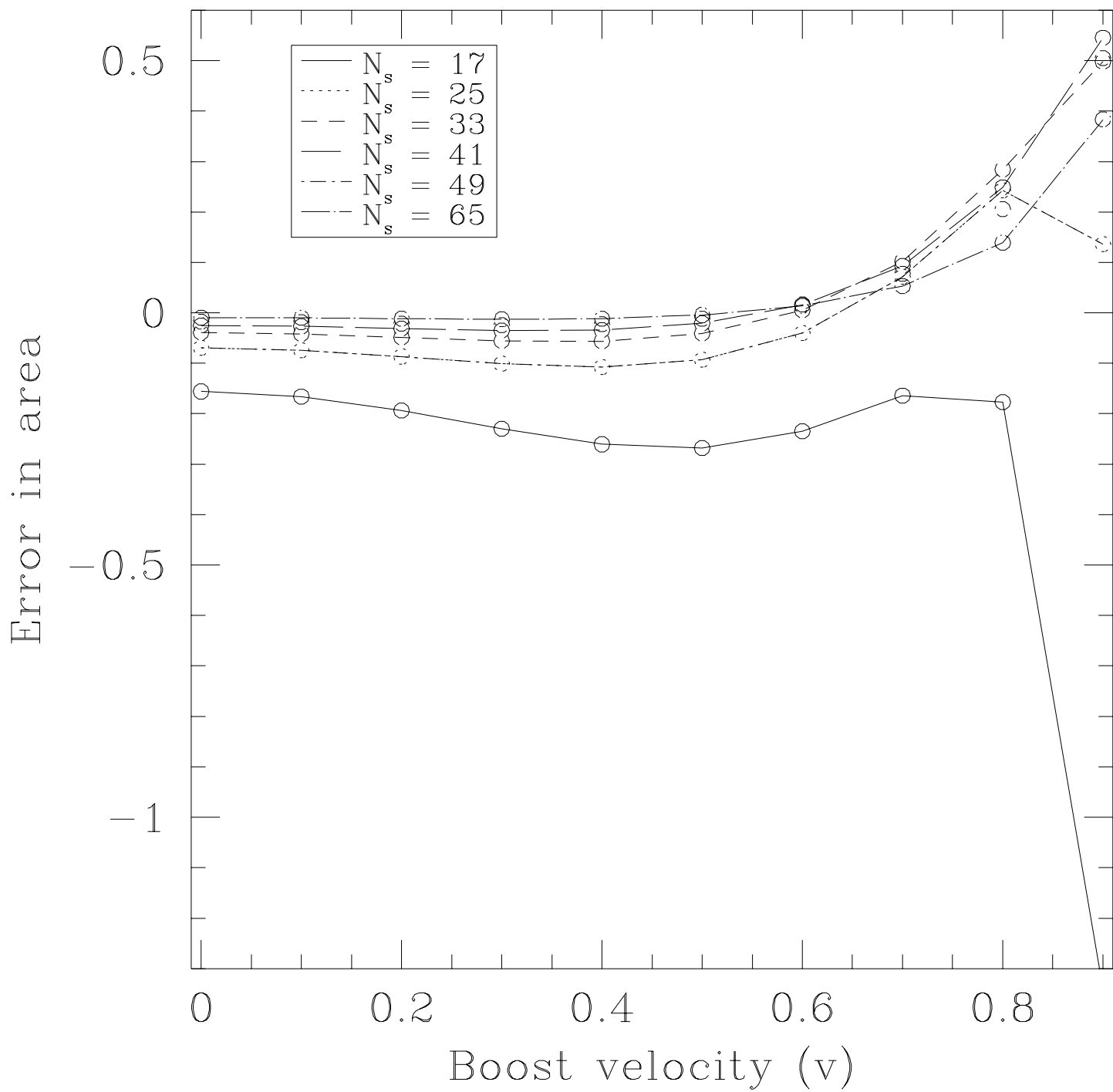


FIG. 11. This figure shows the error in the areas of apparent horizons found for a Schwarzschild black hole boosted in the  $y$ - $z$  direction.

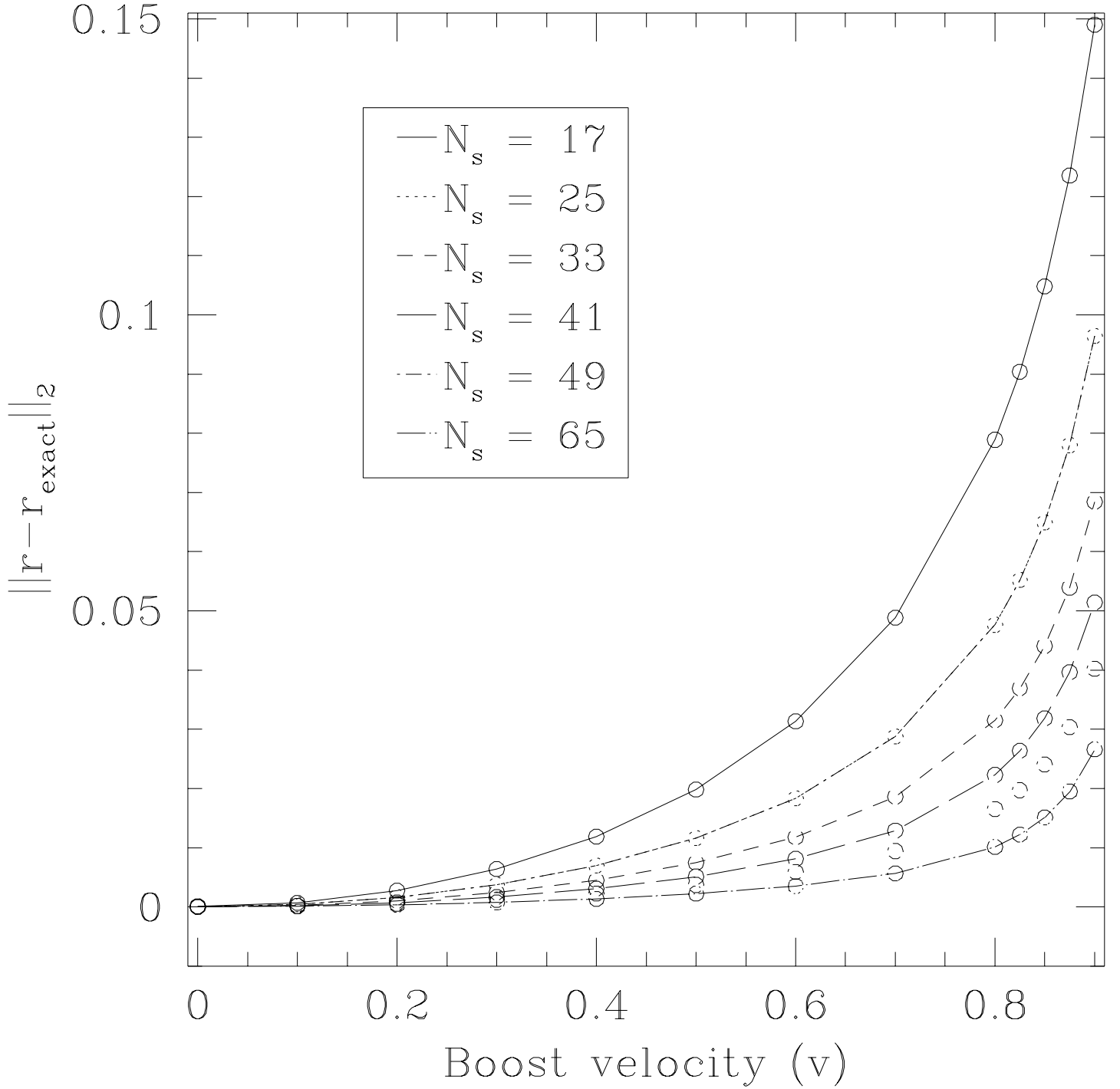


FIG. 12. This figure shows the error in the radial coordinate location  $r = 2M$  for a Schwarzschild black hole apparent horizon for  $v = 0.0, \dots, 0.9$ . The black hole is boosted in the  $xyz$ -direction.

FIG. 13. This figure shows plots of the apparent horizon for the  $a = 0.0$  runs for  $v = 0.0, 0.3, 0.6$  and  $0.9$  for boosts in the  $xyz$ -direction. The mesh used to find the apparent horizon is shown from a top perspective. As the boost velocity is increased we see that the surface is contracted in the  $xyz$ -direction.



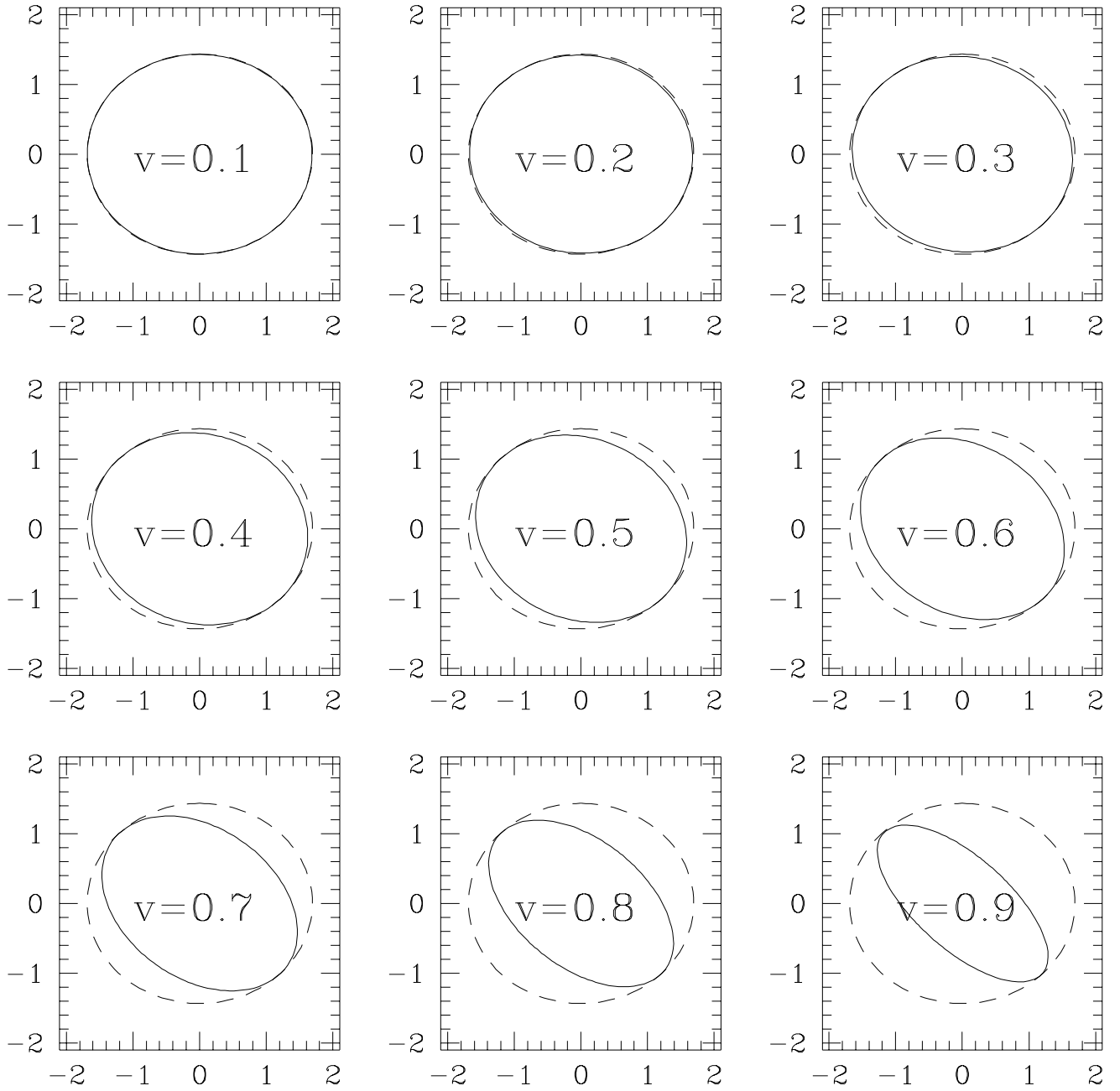


FIG. 14. This figure shows the  $y$ - $z$  cross-section of Kerr ( $a=0.9$ ) black hole apparent horizons located for boost velocities of  $v = 0.0, 0.1, \dots, 0.9$  in the  $y$ - $z$  direction. The dashed circle in each of these figures is the apparent horizon for an unboosted Schwarzschild black hole. Note that the point of contact is along the  $y$ - $z$  direction orthogonal to the direction of the boost.

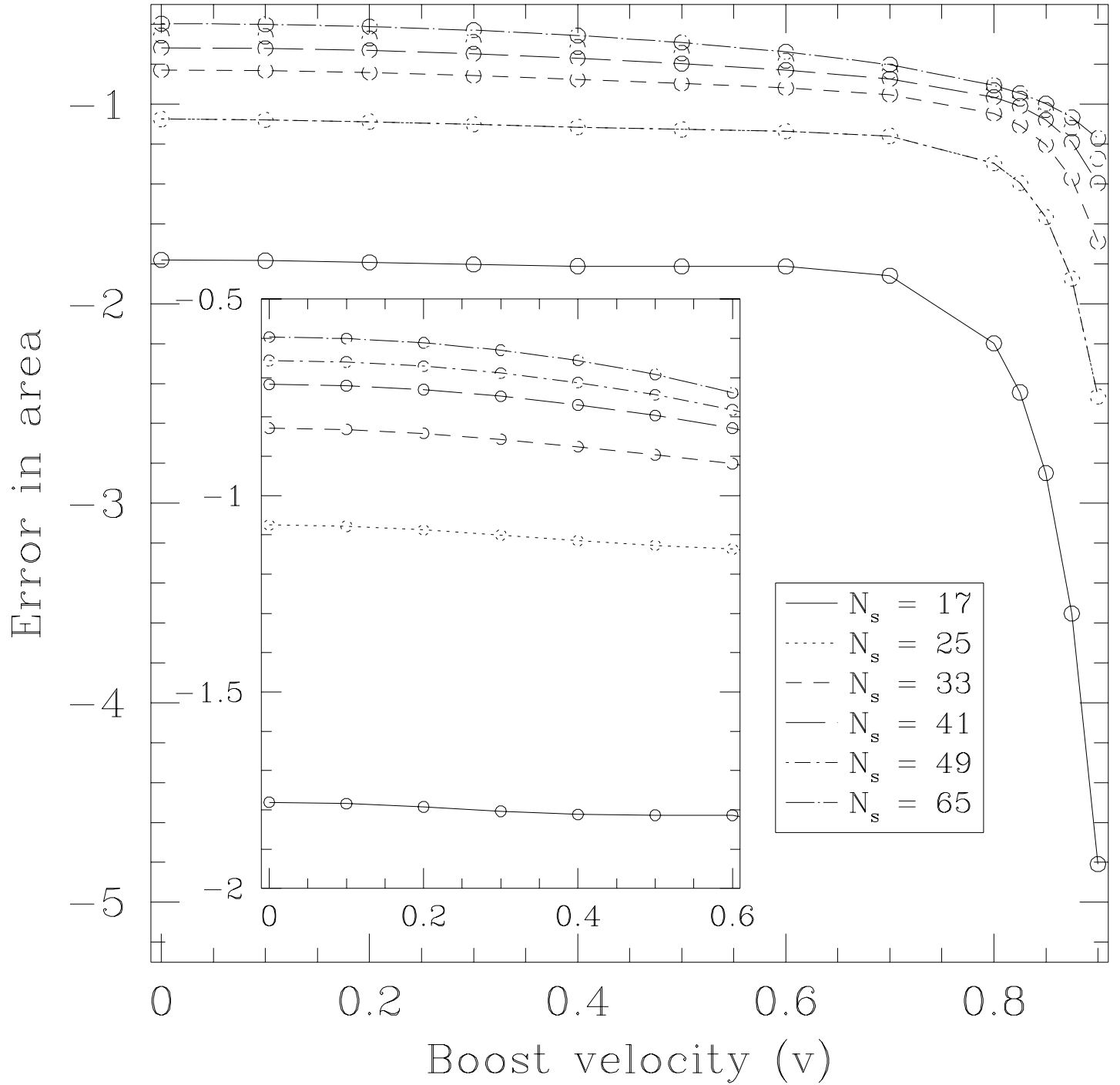


FIG. 15. This figure shows the error in the areas of apparent horizons found for a Kerr black hole boosted in the  $y$ - $z$  direction with  $a = 0.9$ .

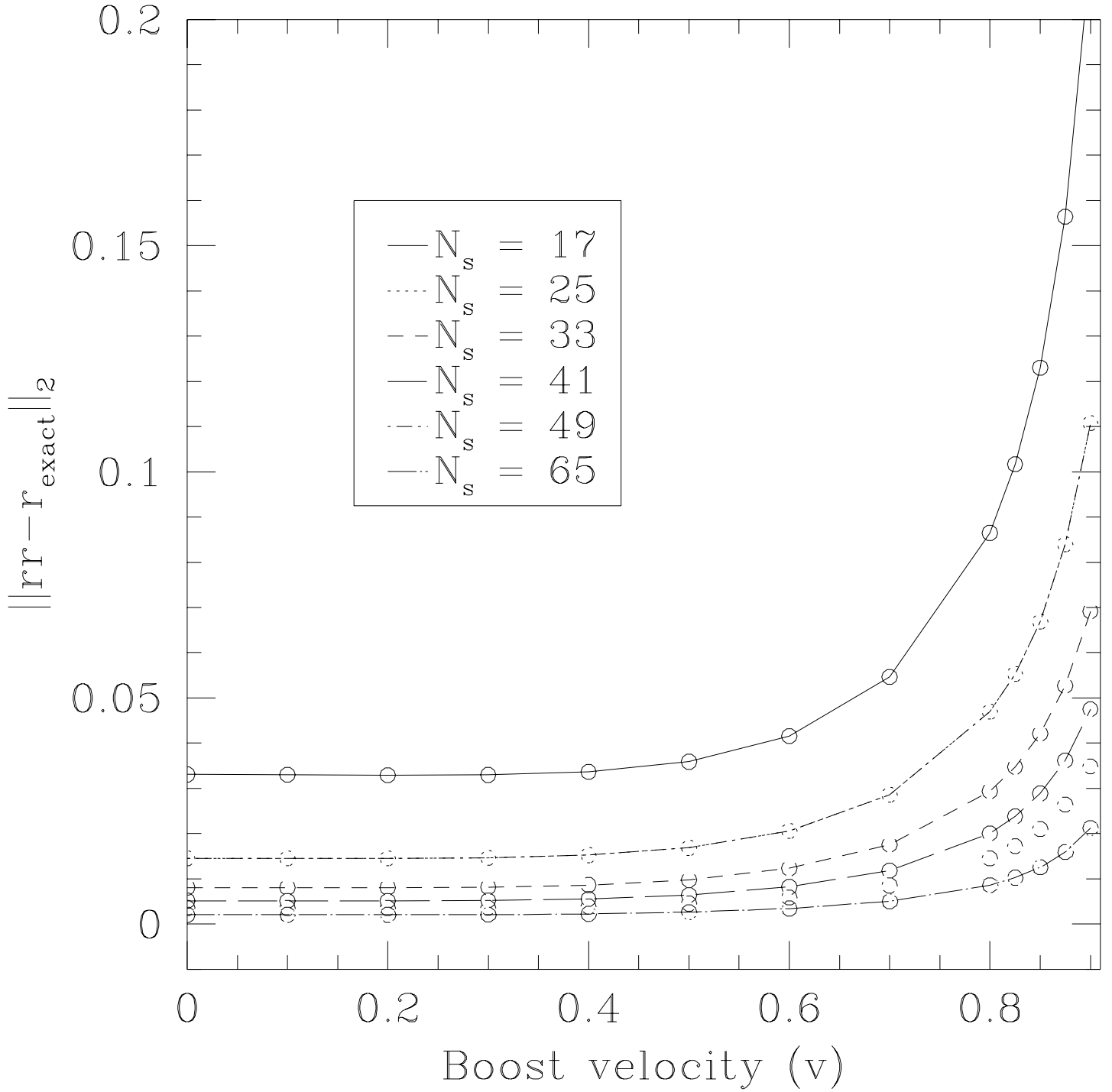


FIG. 16. This figure shows the error in the spheroidal radial coordinate location  $r = r_+$  for a Kerr black hole apparent horizon ( $a = 0.9$ ) for  $v = 0.0, \dots, 0.9$ . The black hole is boosted in the  $xyz$ -direction.

FIG. 17. This figure shows plots of the apparent horizon for the  $a = 0.9$  runs for  $v = 0.0, 0.3, 0.6$  and  $0.9$  for boosts in the  $xyz$ -direction. The mesh used to find the apparent horizon is shown from a top perspective. As the boost velocity is increased we see that the surface is contracted in the  $xyz$ -direction.

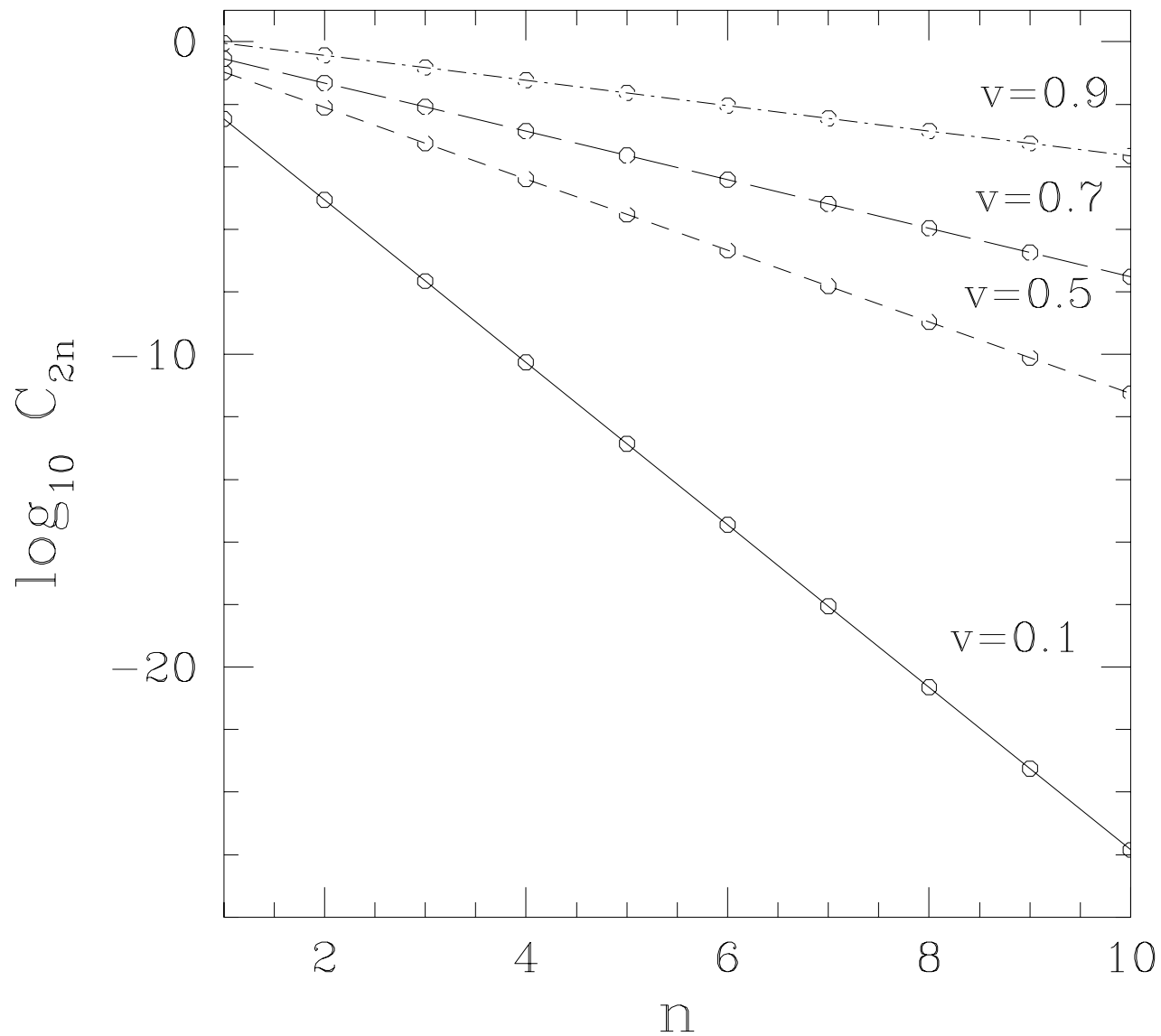


FIG. 18.  $\log_{10}(C_{2n})$  for  $n = 1$  to  $10$  are shown for  $v = 0.1$ ,  $v = 0.5$ ,  $v = 0.7$  and  $v = 0.9$ . The coefficients scale as  $e^{-kn}$  where  $k$  is determined by the shape of the horizon. For  $v = 0.1$  we have  $k \sim 6$  and for  $v = 0.9$   $k \sim 0.9$ .

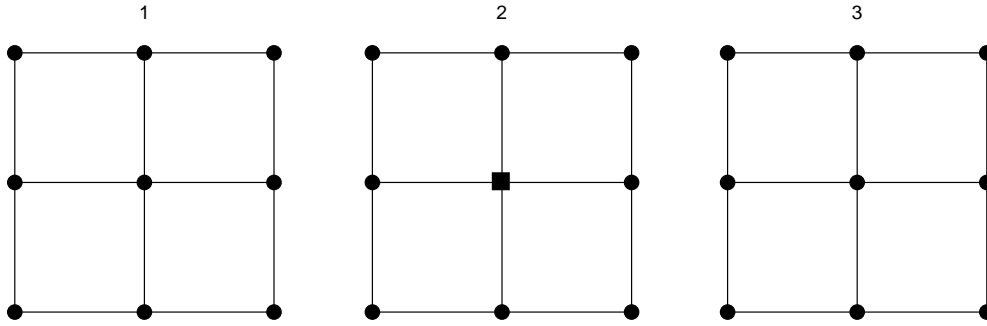


FIG. 19. This figure shows 3 planes of the finite difference molecule  $\mathcal{N}$ . Plane 2 is the center plane with  $z = z_0$ . The center point is denoted by a filled square which is the mesh point  $(x_0, y_0, z_0)$ . Each of the other stencil points in plane 2 are a distance  $\pm\delta x$  and  $\pm\delta y$  away and are denoted by circles. Plane 1 is at  $z = z_0 - \delta z$  and plane 3 is at  $z = z_0 + \delta z$ .

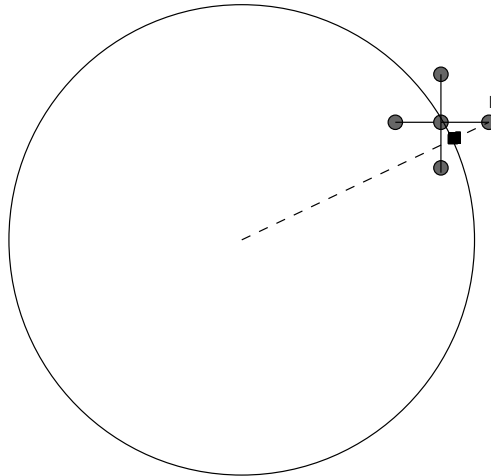


FIG. 20. P is the point at which we wish to estimate  $\varphi$ . The dashed line is the radial line from the origin of our spherical coordinate system to P. The filled square on the surface is the interpolation point where we evaluate  $\rho(\theta_x, \phi_x)$ .

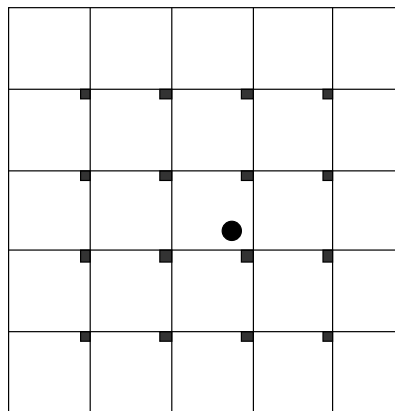


FIG. 21. This figure shows the choice of stencil points that we use for biquartic interpolation for interpolation points that are on the interior of the grid. The interpolation point is labelled by a filled circle and the mesh points that are used as an interpolation stencil are denoted by filled squares.

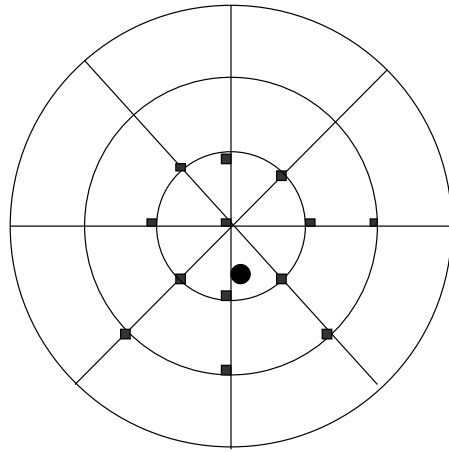


FIG. 22. This figure shows the choice of stencil points for biquartic interpolation for interpolation points that are near the poles. We view the pole points from a 3Dimensional perspective where the identifications of points in the  $\phi$ Direction is taken into account. This leads to the special choice of interpolation stencil points as shown. This leads to fourth order truncation error in the interpolant at the poles. The interpolation point is labelled by a filled circle and the mesh points that are used as an interpolation stencil are denoted by filled squares.

This figure "fig13.gif" is available in "gif" format from:

<http://arxiv.org/ps/gr-qc/0002076v1>

This figure "fig17.gif" is available in "gif" format from:

<http://arxiv.org/ps/gr-qc/0002076v1>